Published in final edited form as:
J Magn Reson Imaging. 2023 June ; 57(6): 1621–1640. doi:10.1002/jmri.28624.

QSM throughout the body

Alexey V. Dimov, PhD[1], **Jiahao Li, BS**[1], **Thanh D. Nguyen, PhD**[1], **Alexandra G. Roberts, MS**[1], **Pascal Spincemaille, PhD**[1], **Sina Straub, PhD**[2], **Zungho Zun, PhD**[1], **Martin R. Prince, MD, PhD**[1], **Yi Wang, PhD**[1]

[1]Department of Radiology, Weill Cornell Medicine, New York, NY, United States

[2]Department of Radiology, Mayo Clinic, Jacksonville, FL, United States

Abstract

Magnetic materials in tissue, such as iron, calcium, or collagen, can be studied using quantitative susceptibility mapping (QSM). To date, QSM has been overwhelmingly applied in the brain, but is increasingly utilized outside the brain. QSM relies on the effect of tissue magnetic susceptibility sources on the MR signal phase obtained with gradient echo sequence. However, in the body, the chemical shift of fat present within the region of interest contributes to the MR signal phase as well. Therefore, correcting for the chemical shift effect by means of water-fat separation is essential for body QSM. By employing techniques to compensate for cardiac and respiratory motion artifacts, body QSM has been applied to study liver iron and fibrosis, heart chamber blood and placenta oxygenation, myocardial hemorrhage, atherosclerotic plaque, cartilage, bone, prostate, breast calcification, and kidney stone.

INTRODUCTION

Quantitative susceptibility mapping (QSM) (1–4) recovers local tissue susceptibility from the nonlocal fields generated by susceptibility sources in gradient echo (GRE) or balanced steady-state free precession (bSSFP)(5) MRI through 1) saving phase in data acquisition and 2) performing spatial deconvolution according to the dipole field model in magnetism physics (6–8). To date, QSM has been performed overwhelmingly in the brain (2,3,9–13), and has seen increased adoption in a variety of brain research protocols to study iron (14–21), myelin (22–25) and calcification (26,27), as well as in clinical protocols such as presurgical mapping of deep brain stimulation targets (28–32). However, QSM has seen also increasing use throughout the body, which is the focus of this review.

There are important biomedical interests to study 1) paramagnetic tissue iron, including deoxyhemoglobin which inversely correlates with oxygen saturation, iron stored in ferritin for iron overload in the liver (33,34) and iron stored in hemosiderin from hemorrhages in atherosclerotic plaques (35,36), 2) diamagnetic tissues, including bone, various pathologic calcifications (37,38), and fibrosis (39), particularly in evaluating tissue damage. QSM has been developed and applied to study neck carotid plaque (40), spine (41–43), breast calcification (44), cardiac oxygenation (45,46), mitral annulus calcification (47) and

---

Corresponding author: Yi Wang, PhD, 407 E 61st, Suite RR118, New York, NY, 10021, USA, yiwang@med.cornell.edu.

hemorrhage, liver iron content (48–50) and fibrosis (51,52), kidney fibrosis (53), cysts and stones, prostate calcification (47), knee cartilage (54,55), and skeletal bones (41,43,56).

There are substantial technical challenges in performing QSM in the body outside the brain in both data acquisition and data processing. For data acquisition, cardiac and respiratory motion effects have to be minimized using motion correction strategies. For data processing, there are two major additional challenges compared to brain QSM. First, GRE phase includes contribution from electron cloud shielding or chemical shift of protons in fat. Accordingly, fat-water separation is performed to remove chemical shift effects before QSM dipole deconvolution. Second, the presence of strong susceptibility sources within or near the region of interest requires special care where conventional dipole deconvolution methods can perform poorly.

This body QSM review consists of two parts. The first is an overview of technical developments common to all body applications. As each organ presents varying technical demands and unique clinical questions, organ specific discussions are presented in the second part, which include liver, atherosclerotic plaque, heart, cartilage and skeletal bones, prostate, breast, kidney and in utero fetus.

TECHNICAL CONSIDERATIONS

Compared to brain applications, the framework of QSM remains conceptually the same in body applications. However, there are crucial differences in how data should be acquired and pre-processed before susceptibility maps can be reconstructed via dipole deconvolution (Figure 1). This body QSM technique overview discusses the following factors in the body affecting the formation of the GRE signal: 1) common occurrence of fatty tissues; 2) nonrigid displacement of organs due to respiratory and cardiac motions, and 3) large dynamic range of susceptibility and presence of tissues with very short transverse relaxation times.

Chemical shift of fat in QSM

Unlike the brain where most of the signal-generating protons are hydrogen nuclei in water, soft tissues elsewhere in the body additionally contain signal-generating protons in fat. Fat molecules consist of three fatty acids connected by means of ester bonds to one glycerol (triglycerides). In these molecules, the external magnetic field B_0 polarizes molecular electron clouds, inducing a shielding magnetic field that alters the field experienced by its protons. As the result, these shielded protons exhibit a different resonance frequency, and its offset relative to water is commonly referred to as chemical shift. Depending on protons' positions within a triglyceride, different protons experience different degrees of electron shielding and hence different chemical shifts forming a chemical shift spectrum. The main peak of the fat chemical spectrum, which accounts approximately for 80% to 90% of the overall signal (57), is offset roughly by $f_c = -3.5$ ppm relative to the resonance frequency of water, or −440Hz at 3T and −220Hz at 1.5T.

The presence of chemical shift poses a significant challenge for mapping the magnetic field generated by local tissue magnetization (tissue field), a foundational step in QSM.

In case of only water in brain (single species), the phase of GRE signal is modeled as a product of tissue field and echo time, and tissue field is estimated from acquired multiple echo GRE data, using a nonlinear least-squares (58) or weighted averaging. Due to the shielding effect described above, the fat signal phase model needs to include chemical shift, in addition to the tissue field. When fat and water coexist within the same voxel (two species), behavior of the GRE signal phase becomes a nonlinear function of tissue field and echo time. Consequently, assuming a single species phase model will result in a field map with unphysical discontinuities at the boundaries between water- and fat-based tissues, preventing meaningful QSM reconstruction (Figure 1, yellow arrows).

Several algorithms exploiting the phase shifts due to the difference in water and fat resonance frequencies have been developed to perform simultaneous mapping of water, fat and magnetic field, which is known as water-fat separation (59–62). Fundamentally, water-fat separation is a nonconvex nonlinear minimization problem that suffers from a) local convergence and heavy dependence on the initialization and b) sensitivity to noise in data. For example, multiple distinct off-resonance or field values can satisfy signal model but only one is the true field value (63). Improper determination of the field value can lead to water and fat being swapped in the output water and fat images, and non-physical discontinuities in the output field map. Accordingly, regularization including the field smoothness is used to constrain the minimization. In classical IDEAL approach (64), smoothness is enforced through convolution of the estimated field with a smoothing kernel at each iteration; the major weakness of this method is its inability to guarantee proper convergence if very strong field inhomogeneities are present. To address this shortcoming, region growing approach (63,65–69) has been proposed. First, several seed voxels within the ROI are heuristically selected. Then, adjacent voxels are iteratively added by minimizing the difference in phase error with all previously added voxels. This region growing approach allows local enforcement of field smoothness, but is computationally greedy with convergence not guaranteed and dependent on the growth path (70). As an alternative to region growing, the graph-cut optimization that inherently optimizes entire volume of interest has been proposed (71–77).

To reinforce the performance of the aforementioned algorithms, robust initialization of the field inhomogeneity map has been accomplished through use of strategically acquired subset of in-phase (IP) echo times (Figure 2) (41,78). The IP echoes are characterized by the constant angle between water and fat components, and can be realized with the echo spacing $\Delta TE = 1/f_c$. IP may introduce constraints on the obtainable readout resolution and/or field of view, which can be alleviated by using higher acquisition bandwidth and bipolar readout gradients.

Recent advances in deep learning (DL) MR image reconstruction brought forth novel methods for water-fat separation and to estimate chemical-shift-free field maps (79–85). DL reconstruction is fast, eliminates the need for initial guess and reduces dependence on acquisition parameters while improving signal to noise ratio (SNR) of reconstructed maps (79,80). However, this approach requires large training sets to sufficiently capture data characteristics and prevent generalization errors.

Data acquisition

Among the existing GRE acquisition schemes, Cartesian (40,45,47,49,55,86,87) and spiral (43,46,88–90) have been primarily used in body QSM applications. Cartesian GRE is widely available on most modern scanners, which makes it a primary choice for clinical imaging and research; however, inefficient k-space sampling limits its application primarily to breathhold imaging (e.g., in liver), musculoskeletal and pelvic MR where breathing motion is not of primary concern. Motion sensitivity of the Cartesian GRE can be mitigated through prospective electrocardiographic (ECG) and diaphragmatic navigator gating (91,92).

To accelerate the acquisition, more efficient spiral k-space sampling, such as variable density stack-of-spirals and cone (93,94), can be employed. Two key benefits of spiral acquisition are very short minimum echo time, which enables ultra-short TE (UTE) imaging of tissues with very short T_2^* (88,89,95), and accelerated acquisition through high k-space undersampling efficiency (96). Additionally, spiral imaging provides motion robustness and intrinsic flow compensation, which are critical in body imaging to mitigate respiratory/cardiac movements and blood flow artifacts. However, spiral images may contain artifacts caused by gradient imperfections, eddy currents, concomitant fields and off-resonance due to B_0 inhomogeneity (97) or chemical shift (98).

Besides the choice of the sequence, the following points should be considered for successful acquisition of data compatible with body QSM applications.

1. Repetition time. Because the quality of QSM hinges upon the quality of the field map, a readout with sufficiently long TR to allow sufficient phase accrual at large TE is recommended. To maximize SNR in field maps, last acquired echo time should be on the order of T_2^* of the tissue of interest (99). To accommodate this requirement, for most of the soft tissues throughout the body TR between 15–20 ms appears to be sufficient (45,47,86,100) at 3 T, with the exception of liver where, due to prevalence of high iron accumulation and fibrosis, shorter TRs (~8–10 ms at 3T) are typically used (48,50,52,101).

2. Number of echoes. Water/fat separation involves fitting of complex data with the minimum of 5 real-valued parameters. Therefore, a minimum of 3 echoes is required for successful field mapping, although higher number of echoes is typically acquired (6 echoes).

3. Imaging resolution and acquisition time. Due to respiratory motion, acquisition of GRE in abdominal imaging calls for a compromise between scan time and image resolution. Thus, breath-holding commonly used in liver imaging limits acquisition times to under 30s, allowing acquisition of 20–30 slices with typical slice thickness of 3–5 mm. Usual in-plane resolution is ~$(1.5 - 2) \times (1.5 - 2)$ mm^2, parallel imaging acceleration factor ≥2, receiver bandwidth ≥300 Hz/pixel.

   Navigator gating can be used for free-breathing acquisitions to increase coverage and resolution, and ECG triggering should be considered for cardiovascular applications. Efficient navigator gating algorithms are important to keep the acquisition time tolerable.

4. Flow compensation. Strong blood flow causes phase variations that can lead to erroneous magnetic field estimates. To mitigate flow-related issues, full flow compensation (102) can be used for cardiovascular QSM.

QSM reconstruction

Magnetic field map estimated from GRE data reflects the total magnetic field experienced by proton spins, which is the superposition of the local tissue magnetic field, generated by susceptibility sources within the chosen region of interest (ROI), and the background field, generated by susceptibility sources outside the ROI. The traditional paradigm of QSM reconstruction consists of two separate steps (1): (a) background field removal to determine the tissue field, and (b) dipole field inversion to obtain the susceptibility map from the tissue field. Multiple algorithms have been developed to filter out background field (103–108), and all of them have demonstrated robust performance in brain imaging; however, technical challenges arise in their translation to body QSM.

First, the large susceptibility differences cross air-tissue interfaces (e.g., at the lung-liver boundary) give rise to very sharp gradients in magnetic field within tissues. These cause a rapid signal decay and make it difficult to measure the total field and separate the background and tissue field (107). Consequently, in the dipole inversion step, the resulting residual background field results in non-local shadow artifacts in the estimated susceptibility map (107,109). To prevent this error propagation, erosion of the tissue mask at the air-tissue interfaces is often required in tissue field dipole inversion, which may prevent visualization of the entire tissue volume, for example, in the superior portion of the liver due to its proximity to diaphragm.

Second, areas with low SNR (bones, ferritin- and hemosiderin-rich ROIs, imperfectly masked air cavities) result in amplified noise during dipole inversion, manifesting as streaking artifacts (109–112). Using a nonlinear QSM model can reduce these streaking artifacts (58), but does not eliminate them. One approach to this challenge is to separate the fitting processes for sources of strong (bone, air) and weak (soft tissues) susceptibilities, hence preventing artifact from permeating into the region of interest (110,113). However, this approach requires careful choice of the regularization parameters, thresholds for detecting low SNR regions.

Tissue field inversion has been successfully used in multiple body applications (48,86,114), but its performance is confounded by sensitivity to strong susceptibility sources within ROI or strong residual background fields. To avoid these sources of error, total field inversion (TFI) has been proposed to handle large dynamic ranges in susceptibility (43,115,116). The key idea of TFI is to adapt the iteration step-size according to the initially estimated susceptibilities (preconditioning) so that the solver converges for a wide range of susceptibility values in a similar number of iterations (115). TFI is capable of properly mapping broad range of susceptibilities over the entire ROIs including soft parenchymal tissues, bones, air-filled cavities and subcutaneous fat. The preconditioner in TFI should conform to magnitudes of underlying sources and can be derived from R_2^* without acquisition of additional data.

ORGAN SPECIFIC CONSIDERATIONS

We review here QSM studies of specific organs in the body: liver, heart, atherosclerotic plaque, musculoskeletal system, prostate, kidney, breast, placenta, and fetus, approximately ordered according to the number of publications. Two aspects are emphasized, 1) biomedical justifications for studying tissue magnetic susceptibilities in these organs and 2) primary findings from these studies.

Liver

Liver produces the majority of proteins involved in iron metabolism, including hepcidin and transferrin, and is the only organ whose iron content is consistently increased in all forms of systemic iron overload (117). Iron overload in the human body occurs in a wide spectrum of conditions, including increased dietary absorption in hereditary hemochromatosis, transfusional hemosiderosis (in thalassemia major, sickle cell disease and refractory anemias) and alcoholic cirrhosis (34,117). Excess iron in hepatocytes catalyzes the formation of highly reactive hydroxyl radicals, which cause cell membrane damage and protein denaturation. Chronic oxidative damage to hepatocytes induces activation of hepatic stellate cells and their differentiation into myofibroblasts, resulting in in collagen deposition, fibrosis and micronodular cirrhosis (118). Since the human body cannot actively eliminate excess iron (119), treatment with chelating agents is required to restore normal body iron levels. Deferoxamine, deferiprone and deferasirox are the most important specific US FDA-approved iron chelators (120). These agents form a water-soluble complex with iron, reducing its reactivity and promoting its excretion. Management of chelation therapy requires constant monitoring to prevent over-chelation and associated adverse effects due to chelator toxicity (121,122).

Due to the linear relationship between tissue magnetic susceptibility and deposition of iron and no need for empirical calibration, QSM of the liver has seen considerable growth of interest over the recent years (48–52,78,101,123). QSM using background field removal and a dipole inversion technique for liver iron measurement has been shown to have high diagnostic performance, with area under the curve (AUC) of 0.948, 0.970, 1, and 1 at susceptibility cut-off values corresponding to liver iron content thresholds of 1.8, 3.2, 7.0, and 15.0 mg/g dry weight (123). It has also been validated against FDA-approved R_2-based method known as Ferriscan (49) and superconducting quantum interference device (SQUID) (48,50). Strong correlations were found between the liver parenchymal susceptibility value and Ferriscan ($R^2 = 0.76$ at 1.5T, $R^2 = 0.83$ at 3T), and between susceptibility and SQUID ($R^2 = 0.82$ at 1.5T, $R^2 = 0.81$ at 3T). Both of these results demonstrate that QSM data can provide good estimates of the liver iron content (Figure 3). In chronic liver disease, it has been demonstrated that QSM has high diagnostic performance in differentiating significant from non-significant hepatic fibrosis (AUC = 0.836). This was further improved by combining QSM, proton density fat fraction (PDFF), and R_2^* (AUC = 0.933) (52). Similar results were also obtained in an imaging study performed on 19 ex vivo samples of liver tissue with further histologic validation; in this work, a combination of QSM and R_2^* resulted in AUC of 0.91 in detecting fibrosis (51).

One of the main technical limitations of QSM in liver iron measurement is decreased performance in the presence of severe iron overload (iron content>27.5 mg/g dw) which precludes acquisition of meaningful GRE signals at conventional echo times (123). Development of advanced acquisition techniques (95,124) is required for full range quantitative liver iron content assessment with QSM.

Heart

QSM has been used to measure differential blood oxygenation between the left and right cardiac chambers (ΔSO_2)(125). This is an established measure of cardiac function: left ventricular (LV) dysfunction results in lower supply of blood to any given organ and thus increases the relative extraction of oxygen from blood. This in turn results in the delivery of more deoxygenated blood to the heart. Increased ΔSO_2 predicts poor prognosis in patients with heart failure with and without pulmonary hypertension (126–128) where it is used to guide treatment (129). The gold standard for measuring this oxygenation based index is invasive catheterization (130) which entails procedural risks and can be challenging in critically ill patients (131,132). Early methods for measuring oxygenation using phase have relied on vessel geometry assumptions (133) that are not applicable to the cardiac chambers. Traditional MRI approaches for chamber oxygenation based on relaxation times (T_2, T_2^*, and T_1) (134–141) can be challenging to apply clinically. In the case of T_2, for example, the dependence of spin echo T_2 on oxygenation is well understood to be complex (142) and in practice requires calibrating several model parameters in addition to oxygenation, potentially affecting accuracy and complicating clinical implementation. Recently, multiple measurements to estimate all parameters in in the complex T_2 model was proposed to overcome the assumptions/calibration of previous T_2 based methods but at the cost of increased scan time (143,144). Instead of relying on modeling the complex relaxation effect of oxygenation on the MR signal magnitude, modeling the magnetic susceptibility of blood on MR signal phase is advantageous because the physical model relating blood susceptibility to oxygen saturation is simpler than that for T_2: it is linear with the known physical constant as slope. Cardiac QSM (45,125) allows mapping of the susceptibility throughout the entire volume containing the heart. Typical acquisitions use an ECG triggered navigator 3D Cartesian mGRE free breathing sampling (Figure 4). The QSM reconstruction is based on TFI (115) which uses an additional regularization constraining the variation of susceptibility in the left as well as the right ventricular chamber, which are segmented before QSM is computed (Figure 5). This regularization is similar the CSF regularization used in MEDI+0 (145), and immediately allows calculating the left-right ventricular ΔSO_2. This method was validated in patients against right heart catheterization, the gold standard for oxygenation (125).

In patients with mitral regurgitation, mitral annular calcification (MAC) negatively impacts the outcome in percutaneous mitral repair (146) especially in advanced MAC (147). QSM is sensitive to calcium as a diamagnetic compound (148). While computed tomography (CT) is reference measurement for MAC, it requires ionizing radiation exposure and cannot measure mitral regurgitation as in MRI. In a study of 24 patients (149), a good agreement was found between a MR based calcium moment (defined as the sum of all susceptibilities in a given ROI) and the conventional calcium score derived from CT obtained in the same patients

(Figure 6). ROC analysis demonstrated an AUC of 0.95 for identifying advanced MAC using cardiac QSM, for which a threshold value of −260.33 ppm×mm^3 lead to a sensitivity of 100% and specificity of 85% in relation to the reference standard of CT.

Reperfusion injury may follow treatment after a heart attack and can lead to reduced heart function and ultimately heart failure. A recent study using a variety of histological and spectral methods established that iron as a biomarker for reperfusion injury in a large animal model (150). Magnetic susceptibility was shown to be closely associated with the duration of coronary artery occlusion, and paramagnetic shift ($\Delta\chi$ > 30 ppb) of infarcted regions relative to distant myocardium was demonstrated in animals with longer time-to-reperfusion, as well as those specimens that did not undergo reperfusion after myocardial infarction. This study also demonstrated myocardial QSM: 1) improved sensitivity for iron without the confounding factors such as edema and fibrosis in conventional cardiac MRI; 2) had greater AUC (0.92) than T_2^* and R_2^* (0.71) in ROC analysis and showed superior balance between sensitivity and specificity of classification.

Carotid atherosclerotic plaque

The carotid bifurcation is a frequent site for progressive formation of atherosclerotic plaques that, when ruptured, produce thromboemboli causing ischemic stroke (151). Currently, high-stake decisions about carotid revascularization as first-line treatment to prevent stroke in patients with stroke or transient ischemic attack symptoms are primarily based on whether there is a ^{3}50% carotid stenosis. However, large randomized controlled trials (152–154) have established that carotid endarterectomy (CEA) is only moderately beneficial for those with 50–69% stenosis compared to noninvasive medical therapy, and many carotid vessels implicated in stroke do not have a >50% stenosis (155,156). Stroke risk from a luminal stenosis can be improved by additional assessment of plaque components: 1) the presence of intraplaque hemorrhage (IPH) has been associated with a 4 to 6-fold increase in stroke risk (35,36) and is a better predictor than all traditional clinical risk factors (157); 2) calcification in carotid plaques has been associated with a 50% lower stroke risk (158). In the conventional multi-contrast MRI approach (159–162), IPH is detected as a hyperintense region on T_1w image, which is attributed to the T_1 shortening effect of paramagnetic methemoglobin associated with the early acute stages of hemorrhage (163,164). However, hemosiderin, an iron storage compound often associated with chronic hemorrhage, has much larger magnetic susceptibility than methemoglobin, resulting in T_1w hypointensity due to field inhomogeneity induced signal loss. This hypointensity increases with the main field strength (165) and can be misinterpreted as calcification, which may lead to stroke risk underestimation. QSM is a sensitive imaging tool for resolving the ambiguous T_1w hypointensity of calcification versus hemosiderin by directly measuring the magnetic susceptibility that induces the hypointensity (166). Therefore, QSM is emerging to be a very valuable addition to multi-contrast MRI for improving carotid plaque characterization and ultimately stroke risk prediction.

Several pilot carotid plaque QSM studies have demonstrated feasibility. One in vivo QSM study of seven patients undergoing CEA showed that QSM yielded substantially improved contrast between IPH and calcification as well as lipid-rich necrotic core (LRNC), which were confirmed by the gold standard histopathology on ex vivo CEA specimens, compared to traditional MRI contrasts (167). These findings agreed well with an ex vivo QSM study of excised CEA samples, which found that calcification and fibrous matrix were prevalent in QSM hypointense areas with negative susceptibility, while IPH and hemosiderin deposition were seen only in QSM hyperintense areas with positive susceptibility (168). Another study of 15 carotid patients found a good agreement in IPH detection between QSM and T_1w MPRAGE (k = 0.822), as well as similar IPH and calcification area measurements obtained by QSM and conventional multi-contrast sequences (169). They also reported highly reproducible mean plaque susceptibility values in three patients (169). The nonlinear preconditioned TFI algorithm can improve QSM quality and detection of IPH and calcification when using multi-contrast MRI as the reference standard (40). Furthermore, TFI can detect small focal hyperintense areas with high positive susceptibility consistent with IPH that is invisible or appears hypointense on multi-contrast MRI, similar to calcification (Figure 7), enabling IPH to be distinguished from calcification.

Plaque inflammation has been studied through imaging the uptake of nanoparticles by macrophages in the plaque, as shown in a QSM study of the carotid plaques in five patients before and after the administration of ultrasmall superparamagnetic iron oxide nanoparticles as a means to detect inflammation (170). Regions of calcification appeared strongly diamagnetic on both pre-contrast and post-contrast QSM (≈ -1 ppm), while regions of USPIO uptake appeared strongly paramagnetic (>1 ppm). Plaque regions containing neither calcification nor USPIO had susceptibility values close to zero in both pre- and post-contrast QSM images. USPO uptake and presence of calcifications was further confirmed by plaque histology samples obtained in two patients These early findings suggest that QSM has the ability to improve carotid plaque characterization.

Successful clinical adoption of carotid plaque QSM in the future will depend on overcoming several technical challenges. A major challenge is the residual streaking or shadow artifacts in the susceptibility map caused by the proximity of background air, air cavities, fat (171,172), bone, and blood flow in the neck region. Another challenge is the noise amplification in areas with low signal-to-noise ratio such as calcified plaques, especially when data acquisition is performed using a product head/neck coil with less optimal anatomical coverage compared to a dedicated carotid coil (173). Recently developed susceptibility source separation methods (174–177) may be useful for separating co-localizing IPH and calcification in the atherosclerotic plaques. Finally, a multi-contrast acquisition and reconstruction approach that utilizes the shared structural information among different image contrasts to vastly reduce the scan time (178–180) will be essential to translate carotid plaque QSM into a routine imaging workup.

Musculoskeletal and spinal applications.

Due to its sensitivity to magnetic tissue composition and structure, QSM has been successfully applied to study cartilage tissue in in animal models, ex vivo samples, as well as healthy and osteoarthritic subjects at different field strengths (54,55,181–188). The collagen fiber is a major source of contrast in cartilage to assess microstructural pathologies within the collagen matrix (Figure 8A) (183). In healthy cartilage, architecture and biochemical composition of the functional extracellular matrix is strictly maintained by the chondrocytes (189). However, if the balance between the anabolic (synthesis of cartilage matrix components) and catabolic (normal turnover of matrix molecules) processes is disrupted by physical or molecular mechanism, chondrocytes activate in an attempt to repair the matrix. Following up-regulation of matrix synthesis, expression of proteolytic enzymes, increased expression of pro-inflammatory cytokines and tissue necrosis factor alpha leads to clustered apoptosis and proliferation of cells, disrupting integrity of the cellular network (190,191). Cartilage and its surrounding tissues are affected in osteoarthritis (OA), a highly prevalent and slowly progressing degenerative joint disease. The OA changes include subchondral sclerosis, meniscal degradation, osteophytosis, and, as a primary pathologic feature, loss of articular cartilage (192–194) in spinal and peripheral joints. MRI is among the best non-invasive tools available for diagnosis of OA (195).

In the preclinical animal studies, QSM has been shown to be sensitive to progressive degeneration of epiphyseal cartilage canals due to induced chondronecrosis (185); similar ability of QSM to visualize cartilage canals and cartilage vascular architecture in pediatric subjects has been demonstrated (54,181). In equine model of post-traumatic osteoarthritis, combination of QSM and T_2^* within articular cartilage allowed successful prediction of reference parameters (equilibrium and dynamic moduli, proteoglycan content, collagen fiber angle and anisotropy) with high Spearman’s rank correlation ($\rho = [0.49 \ldots 0.68]$) between measured and predicted parameters (187). A prospective quantitative study performed in OA patients demonstrated that the variation of magnetic susceptibility within the knee cartilage was associated with the stage of OA (55). In a more recent study in marathon runners, QSM has been shown to be sensitive to acute changes in femoral and tibial cartilage after repetitive loading without any morphologic changes (184). While more research is required for successful clinical translation of QSM, these findings indicate the potential of susceptibility quantification to provide critically relevant information about structure of cartilage.

Osteoporosis (OP) is a systemic skeletal disease characterized by low bone mass and a consequent increase in risk of fractures (196). The skeleton is metabolically active and undergoes continuous remodeling throughout life, occurring at discrete sites known as basic multicellular units. Each unit is a dynamic structure comprised of osteoclasts, osteoblasts, and osteocytes (197). During bone remodeling, recruited osteoclasts degrade mineralized bone and undergo subsequent apoptosis; after this, osteoblasts are recruited to the site, and formation and mineralization of new bone takes place (197,198). Under normal conditions, the processes of bone resorption and formation are balanced. With age, this balance is disrupted. In post-menopausal women, the rate of bone remodeling is increased, while the remodeling balance becomes negative due to increased osteoclast-mediated bone resorption, resulting in bone overall bone loss; in contrast, ageing in men is associated with reduced bone formation (196,199). Bone mineral density (BMD) assessment using dual energy x-ray absorptiometry (DXA) and quantitative CT (qCT) is central to the diagnosis of OP (200). Because of the widespread use of bone mineral densitometry, there is potential to improve the standards of care if the radiation dose could be minimized by using non-ionizing imaging modalities.

Utilization of magnetic susceptibility as a skeletal MR imaging biomarker is still under active development despite first being proposed about three decades ago (201,202). The main contrast mechanism in bone QSM is deposition of hydroxyapatite, a calcium compound, withing the bone matrix. The main challenge in bone MR is the ultrashort apparent transverse relaxation time (~300 μs) (203) of bound bone water, resulting in no meaningful phase for QSM reconstruction in conventional GRE. To address this challenge, utilization of UTE sequences has been proposed (56,88). In ex vivo specimens, estimated magnetic susceptibility of cortical bone has been found to correlate against μCT-derived BMD and bone porosity (88) and traditional CT Hounsfield units (56), warranting further investigations (Figure 8B). Besides bone density assessment, the feasibility of QSM for detecting hemosiderin deposition in patients with hemophilic arthropathy (89) and for tracking gadolinium-based contrast agents deposition within cortical bone (204,205) have been demonstrated (206).

Spine is an extension of the central nerve system and connects different parts of the musculoskeletal system. Pathologic changes in calcification and hematopoietic bone marrow of the spine can cause changes in magnetic susceptibility, which can be studied using QSM (207,208). Spine QSM can be effectively obtained using an IP acquisition with consecutive tissue field inversion (42). In vivo study comparing vertebral QSM, proton density fat fraction and BMD performed in 108 postmenopausal females found that a statistical model combining QSM and PDFF resulted in high specificity and sensitivity (AUC>0.82) in differentiating normal, oteopenic and osteoporotic subjects (41). QSM has also been demonstrated to be sensitive to osteolytic metastases within the spinal column, surpassing conventional MR sequences (T_1w, T_2w, T_2w-water) in sensitivity (43)

Prostate

Prostate cancer is the most common cancer in men in the US (209). Fiducial markers are used as landmarks for radiation therapy for prostate cancer treatment (210). The workflow for image-based localization of fiducial markers for radiation therapy of the prostate is usually based on CT. However, MRI only workflows are sought for because of the superior soft tissue contrast of MRI compared with CT and because they eliminate the risk for MR-CT registration errors as well as reduce the exposure of patients to ionizing radiation (211–213). Conventional MRI workflows using magnitude data lack the ability to differentiate between diamagnetic calcification that are a common finding in the prostate (214), fiducial markers such as gold fiducial markers that are more diamagnetic than calcification or titanium encapsuled seeds that are strongly paramagnetic, and blood products that possess a paramagnetic susceptibility. Therefore, the risk for error might outweigh the benefits of an MRI-only workflow (211). Moreover, the use of prostatic calcification as an internal fiducial marker has been proposed (212).

A recent study showed that susceptibility values of gold intraprostatic fiducial markers were significantly different from the susceptibility values of intraprostatic calcification ($p < 0.001$), facilitating QSM-based radiotherapy planning and overcoming the limitations of magnitude-based MRI workflows (215). Using an unsupervised k-means and k-medoids clustering machine learning algorithm, QSM-based automated detection of implanted low dose rate brachytherapy seeds could accurately detect seeds and estimate seed centroids while seed orientations were highly correlated with the actual orientations ($R > 0.98$) (213). Preceding the applications to prostate radiation therapy, prostate-QSM has been first used to detect intra-prostatic calcification as well as calcification in the periphery of the prostate (47) (Figure 9) and average susceptibility values were reported to be −0.249 ± 0.179 ppm. For QSM of the prostate, susceptibility values have been referenced to iliopsoas muscle (112,216), or to internal obturator muscles (217).

There can be large air-filled spaces in the vicinity of the prostate dependent on subject physiology, that will create strong artifacts when not considered in background field removal. Furthermore, excluding regions with very short T_2^* relaxation time such as bones, and therefore, unreliable phase data, can improve the quality of susceptibility maps of the prostate (112). While the prostate itself does not contain fat, it is surrounded by different tissues including muscle and fat tissues so that accounting for the chemical shift between water and fat can further reduce shading artifacts (217).

Breast

Breast cancer is the most common cancer in women in the US (209). While large macrocalcifications (218) are often associated with benign conditions such as fibroadenomas, microcalcification can be associated with breast cancer or ductal carcinoma in situ (DCIS) (219). The gold standard for the detection of calcification in the breast is mammography, a projection technique, which may be inferior to 3D imaging modalities such as MRI regarding its localization properties. This might also limit detection in certain instances. However, current clinical MRI protocols lack the ability to detect calcification.

Early on in the history of QSM, it has been shown that QSM of the breast is feasible, it can be used to detect calcification (44,220) (Figure 10), and that it might even provide complementary information about tumor morphology and vascularization compared to mammography or contrast-enhanced imaging (44). Recently QSM-based mammography-like MR images using a preconditioned water-fat-silicone total field inversion algorithm were used to detect smaller microcalcification in the presence of silicone implants (221). Further studies are required to establish diagnostic efficiency of breast QSM and compare its performance against the golden standard of mammography and multiparametric MRI protocols.

Kidney

The kidney possesses a complex geometry comprised of nephrons that are subdivided into vessels, glomerulus and the tubules facilitating its integral functions in the urinary and endocrine systems such as filtration, control of body fluids and hormonal regulation. In a pre-clinical ex vivo study the complex geometry of the kidney could be visualized using susceptibility tensor imaging (222,223).

QSM has been applied to study kidney fibrosis. Chronic kidney disease is characterized by renal interstitial fibrosis for which the standard diagnosis is renal biopsy. Therefore, the interest in finding non-invasive biomarkers has been growing in recent years with great interest in MRI biomarkers (224). It was shown in a pre-clinical study using a mouse model prone to focal interstitial fibrosis, cortical inflammation, glomerulocysts and inner medullary hypoplasia that susceptibility values of the kidneys of wild-type mice were more paramagnetic than in knock-out mice (225). This observation was attributed to an increase in proteins and lipids due to inflammation and fibrosis, which possess a relatively diamagnetic susceptibility. A first feasibility study on healthy volunteers that also included one patient with kidney fibrosis could reproduce the results from the animal study and showed strongly reduced susceptibility values in the fibrosis patient (53).

QSM has been used in the study of autosomal dominant polycystic kidney disease (ADPKD). At present, one of the most commonly utilized biomarkers for prediction of the renal function decline in ADPKD is height-adjusted total kidney volume (ht-TKV) (226–228). However, despite its efficiency, this measure is a surrogate marker which does not take in account many other features of ADPKD and manifestations of kidney injury provided by abdominal MRI. Thus, recent findings suggest that the renal cyst hemorrhage is a significant predictor of rapid disease progression to ESRD (229,230). Cystic hemorrhages are detected as hyperintense on T_1-weighted images acquired as a part of a multi-contrast abdominal MR examination, assuming erythrocytes have lysed releasing mobile iron (164). However, the T_1-weighted signal intensity of hemorrhage is not hyperintense when erythrocytes have not lysed, or iron has been collected into large hemosiderin clusters. Thus, the T_1-weighted signal-intensity of hemorrhagic cysts is complicated and may lead to misdiagnosis.

Kidney stones are common among the chronic kidney disease and ADPKD patients (231–235). Patients with urinary stones should be followed up more closely for progression (234). Non-contrast CT is a highly sensitive and specific technique for imaging kidney stones (236). Once a partially obstructing ureteral stone has been identified on CT, following the gradually descent of the stone down the ureter is not practicable with CT due the cumulative radiation exposure of multiple scans (237). QSM can exploit large differences in magnetic susceptibilities of blood products, mineral depositions, and normal kidney parenchyma to distinguish diagnostic features associated with the disease (Figure 11). QSM offer the potential to follow stones to see if they are progressing to been excreted or if an intervention will be required.

For QSM of the kidney, paravertebral muscle tissue can be used a reference for susceptibility value quantification (53) as well as the whole kidney (225).

Placenta

The placenta is a vital organ for normal fetal development, providing the maternal-fetal interface for oxygen and nutrient exchange. Given the exceptionally high blood volume of the placenta (~50%), magnetic susceptibility measured in the placental tissue using QSM is likely to reflect blood oxygenation and may offer early biomarkers of placental failure. Placental QSM may be performed using 2D/3D single-echo EPI or multi-echo GRE imaging with respiratory gating (114,238,239). While single-echo EPI approach offers an extremely shorter scan time for whole placenta imaging (~10 s), its noise level in field map estimation may be higher than that of multi-echo imaging (114). For both single- and multi-echo approaches, TE must be determined considering relatively longer T_2^* values of the placenta compared to other organs and the decreasing tendency with advancing gestational age (from 70 to 25 ms at 3T in the third trimester) (114) unless iron is of interest (239). In previous studies, standard QSM algorithms were used for background field removal (103,240) and dipole inversion (7,241,242). Amniotic fluid may be used for susceptibility reference similar to the CSF in brain QSM (238,239) although there exist several challenges, such as fully flow-compensated acquisition for amniotic fluid circulation and selection of a large and reliable region in amniotic fluid without operator-dependent bias (114).

Placental QSM has been performed in both healthy pregnancies and those complicated by placental insufficiency (114,238). In healthy pregnancies, the feasibility of placental QSM was demonstrated by showing lobular contrast in susceptibility maps, no difference in susceptibility measures between 1.5T and 3T, increasing spatial variation of susceptibility with advancing gestational age, and sensitivity of susceptibility to induced maternal hyperoxia (Figure 12) (114). Compared to healthy pregnancies, susceptibility of the placentas associated with preeclampsia was found to be higher (238). More importantly, spatial variation of susceptibility was significantly larger with preeclampsia (Fig. 12B) (238). The underlying cause of this spatial variation remains unclear because in principle susceptibility of the placenta is sensitive to many other factors besides blood oxygenation, such as hemorrhage, calcification, and susceptibility of the villous tissues and septa. Nevertheless, placental QSM may offer direct imaging biomarkers of placental insufficiency.

Fetus

While placental oxygenation may serve as an early marker of disrupted fetal development, direct measurement of blood oxygenation in the fetal brain may identify fetuses at immediate risk for hypoxic ischemic injury. Similar to in adult brains, QSM can be used to measure venous oxygenation of the superior sagittal sinus in the fetal brain based on the paramagnetism of deoxyhemoglobin. Earlier studies used only the intravascular phase data with a long cylinder assumption on the superior sagittal sinus(243,244). More accurate measurement of susceptibility using a QSM pipeline was performed in follow-up studies (245,246). For susceptibility measurement in the vasculature, fully-flow compensated GRE imaging is required and relatively short echo times (15–20 ms) are used due to short T_2^* of venous blood. Blood oxygenation can be converted from susceptibility using a simple equation that describes the relationship between the two parameters. In literature, another application of QSM in fetuses was estimation of calcification in the fetal spine (247). Diamagnetic susceptibility of calcium in the fetal vertebrae may be used to assess bone growth and mineralization of the fetus, which may be disturbed in case of maternal hypocalcemia in pregnancy. All these prior fetal QSM studies were performed without sophisticated motion compensation techniques; data acquisition was repeated when fetal motion occurred and images with motion artifacts were excluded from analysis. GRE imaging with a radial or spiral trajectory is a promising approach to reduce fetal motion artifacts and may be explored in future studies(88,89).

Venous oxygenation measured in the fetal superior sagittal sinus using QSM was approximately 65–67% (245,246), which is in good agreement with literature values measured using near infrared spectroscopy (248). Oxygenation was higher in the fetal brain with ventriculomegaly than healthy controls (67.8% vs 65.3%) although the difference was not significant with a small sample size (246). The increased venous oxygenation with ventriculomegaly may suggest reduced oxygen extraction fraction attributed to reduced metabolism with impaired fetal brain function. On the other hand, QSM was also demonstrated to be sensitive to the diamagnetism of calcium in fetuses (247). Susceptibility measured in the fetal vertebrae decreased significantly with advancing gestational age in healthy pregnancies, which may indicate increasing calcium content associated with normal bone development. Fetal QSM is potentially a safe and effective tool to provide early markers of impaired fetal development and may be further investigated in various high-risk pregnancies such as those complicated by fetal heart disease, fetal growth restriction, or preeclampsia.

DISCUSSION AND CONCLUSION

QSM in the body outside the brain needs to account for the fat contribution to the phase signal. Technical advancements in QSM data acquisition and reconstruction have achieved robust water/fat separation, enabling QSM outside the brain. Body QSM has opened a venue for noninvasive study of local tissue magnetic susceptibility properties and their pathological changes.

The following promising body QSM applications have been identified. Liver QSM can provide iron quantification without fibrosis interference suffered by the R_2^* or R_2 based method. Cardiac QSM can provide chamber blood oxygenation quantification noninvasively without relying on complicated magnitude modeling. Atherosclerotic plaque QSM can differentiate calcification components from hemorrhages without the ambiguity in T_1 weighted image intensity. Further exciting developments in body QSM include cartilage and bone quantification in skeleton and spine, calcification mapping in prostate, breast and kidney stone, and oxygenation in the placenta and fetal brain.

Compared to brain QSM, body QSM is less developed and offers wider opportunities for technical and application developments. While studying gross organ properties such as iron content of the liver allows for rapid QSM acquisitions that can be performed within one breath hold, the detection of smaller lesions might in future require acquisition strategies that effectively account for motion during image acquisition. The recent advancements in fast imaging, including deep learning-based acceleration, can be explored and harnessed for body QSM with robustness against motion artifacts (249). These technical developments will facilitate exciting clinical translation research activities, including body QSM applications in studying various diseases and in monitoring various therapy responses.

In conclusion, QSM can be developed and applied to study accumulation or loss of paramagnetic iron, diamagnetic calcium, and structural tissue changes such as diamagnetic fibrosis in all organs in the body beyond the brain.

Grant support:

S10OD021782, R01DK116126, R01HL151686, R21NS116516, R01NS123576-01A1, R01HD100012

References

1. Wang Y, Liu T. Quantitative susceptibility mapping (QSM): Decoding MRI data for a tissue magnetic biomarker. Magn Reson Med 2015;73(1):82–101. [PubMed: 25044035]
2. Harada T, Kudo K, Fujima N, et al. Quantitative Susceptibility Mapping: Basic Methods and Clinical Applications. Radiographics 2022;42(4):1161–1176. [PubMed: 35522577]
3. Vinayagamani S, Sheelakumari R, Sabarish S, et al. Quantitative Susceptibility Mapping: Technical Considerations and Clinical Applications in Neuroimaging. J Magn Reson Imaging 2021;53(1):23–37. [PubMed: 31951057]
4. Haacke EM, Liu S, Buch S, Zheng W, Wu D, Ye Y. Quantitative susceptibility mapping: current status and future directions. Magn Reson Imaging 2015;33(1):1–25. [PubMed: 25267705]
5. Boyacioglu R, Wang C, Ma D, McGivney DF, Yu X, Griswold MA. 3D magnetic resonance fingerprinting with quadratic RF phase. Magn Reson Med 2021;85(4):2084–2094. [PubMed: 33179822]
6. de Rochefort L, Liu T, Kressler B, et al. Quantitative susceptibility map reconstruction from MR phase data using bayesian regularization: validation and application to brain imaging. Magn Reson Med 2010;63(1):194–206. [PubMed: 19953507]
7. Liu J, Liu T, de Rochefort L, et al. Morphology enabled dipole inversion for quantitative susceptibility mapping using structural consistency between the magnitude image and the susceptibility map. Neuroimage 2012;59(3):2560–2568. [PubMed: 21925276]
8. Marques JP, Bowtell R. Application of a fourier-based method for rapid calculation of field inhomogeneity due to spatial variation of magnetic susceptibility. Concept Magn Reson B 2005;25b(1):65–78.
9. Eskreis-Winkler S, Zhang Y, Zhang J, et al. The clinical utility of QSM: disease diagnosis, medical management, and surgical planning. NMR Biomed 2017;30(4).
10. Ravanfar P, Loi SM, Syeda WT, et al. Systematic Review: Quantitative Susceptibility Mapping (QSM) of Brain Iron Profile in Neurodegenerative Diseases. Front Neurosci 2021;15:618435. [PubMed: 33679303]
11. Liu C, Wei H, Gong NJ, Cronin M, Dibb R, Decker K. Quantitative Susceptibility Mapping: Contrast Mechanisms and Clinical Applications. Tomography 2015;1(1):3–17. [PubMed: 26844301]
12. Nikparast F, Ganji Z, Zare H. Early differentiation of neurodegenerative diseases using the novel QSM technique: what is the biomarker of each disorder? BMC Neurosci 2022;23(1):48. [PubMed: 35902793]
13. Bandt SK, de Rochefort L, Chen WW, et al. Clinical Integration of Quantitative Susceptibility Mapping Magnetic Resonance Imaging into Neurosurgical Practice. World Neurosurg 2019;122:E10–E19. [PubMed: 30201583]
14. Langkammer C, Schweser F, Krebs N, et al. Quantitative susceptibility mapping (QSM) as a means to measure brain iron? A post mortem validation study. Neuroimage 2012;62(3):1593–1599. [PubMed: 22634862]
15. de Hollander G, Keuken MC, Bazin PL, et al. A gradual increase of iron toward the medial-inferior tip of the subthalamic nucleus. Hum Brain Mapp 2014;35(9):4440–4449. [PubMed: 24596026]
16. Barbosa JH, Santos AC, Tumas V, et al. Quantifying brain iron deposition in patients with Parkinson’s disease using quantitative susceptibility mapping, R2 and R2. Magn Reson Imaging 2015;33(5):559–565. [PubMed: 25721997]
17. Wisnieff C, Ramanan S, Olesik J, Gauthier S, Wang Y, Pitt D. Quantitative susceptibility mapping (QSM) of white matter multiple sclerosis lesions: Interpreting positive susceptibility and the presence of iron. Magn Reson Med 2015;74(2):564–570. [PubMed: 25137340]
18. Blazejewska AI, Al-Radaideh AM, Wharton S, et al. Increase in the iron content of the substantia nigra and red nucleus in multiple sclerosis and clinically isolated syndrome: a 7 Tesla MRI study. J Magn Reson Imaging 2015;41(4):1065–1070. [PubMed: 24841344]
19. Li KR, Avecillas-Chasin J, Nguyen TD, et al. Quantitative evaluation of brain iron accumulation in different stages of Parkinson’s disease. J Neuroimaging 2022;32(2):363–371. [PubMed: 34904328]

20. Chen L, Soldan A, Oishi K, et al. Quantitative Susceptibility Mapping of Brain Iron and beta-Amyloid in MRI and PET Relating to Cognitive Performance in Cognitively Normal Older Adults. Radiology 2021;298(2):353–362. [PubMed: 33231528]
21. Kaunzner UW, Kang Y, Zhang S, et al. Quantitative susceptibility mapping identifies inflammation in a subset of chronic multiple sclerosis lesions. Brain 2019;142(1):133–145. [PubMed: 30561514]
22. Chen WW, Gauthier SA, Gupta A, et al. Quantitative Susceptibility Mapping of Multiple Sclerosis Lesions at Various Ages. Radiology 2014;271(1):183–192. [PubMed: 24475808]
23. Zhang Y, Gauthier SA, Gupta A, et al. Magnetic Susceptibility from Quantitative Susceptibility Mapping Can Differentiate New Enhancing from Nonenhancing Multiple Sclerosis Lesions without Gadolinium Injection. Am J Neuroradiol 2016;37(10):1794–1799. [PubMed: 27365331]
24. Li X, Harrison DM, Liu H, et al. Magnetic susceptibility contrast variations in multiple sclerosis lesions. J Magn Reson Imaging 2016;43(2):463–473. [PubMed: 26073973]
25. Lambrecht V, Hanspach J, Hoffmann A, et al. Quantitative susceptibility mapping depicts severe myelin deficit and iron deposition in a transgenic model of multiple system atrophy. Exp Neurol 2020;329:113314. [PubMed: 32302677]
26. Deistung A, Schweser F, Wiestler B, et al. Quantitative Susceptibility Mapping Differentiates between Blood Depositions and Calcifications in Patients with Glioblastoma. Plos One 2013;8(3).
27. Chen WW, Zhu WZ, Kovanlikaya I, et al. Intracranial Calcifications and Hemorrhages: Characterization with Quantitative Susceptibility Mapping. Radiology 2014;270(2):496–505. [PubMed: 24126366]
28. Rasouli J, Ramdhani R, Panov FE, et al. Utilization of Quantitative Susceptibility Mapping for Direct Targeting of the Subthalamic Nucleus During Deep Brain Stimulation Surgery. Oper Neurosurg (Hagerstown) 2018;14(4):412–419. [PubMed: 28531270]
29. Rashid T, Hwang R, DiMarzio M, Hancu I, Pilitsis JG. Evaluating the role of 1.5T quantitative susceptibility mapping for subthalamic nucleus targeting in deep brain stimulation surgery. J Neuroradiol 2021;48(1):37–42. [PubMed: 31150663]
30. Dimov A, Patel W, Yao Y, Wang Y, O'Halloran R, Kopell BH. Iron concentration linked to structural connectivity in the subthalamic nucleus: implications for deep brain stimulation. J Neurosurg 2019:1–8.
31. Yu KJ, Ren ZW, Yu T, et al. Direct Targeting of the Anterior Nucleus of the Thalamus via 3 T Quantitative Susceptibility Mapping. Front Neurosci-Switz 2021;15.
32. Wei HJ, Zhang CC, Wang T, et al. Precise targeting of the globus pallidus internus with quantitative susceptibility mapping for deep brain stimulation surgery. Journal of Neurosurgery 2020;133(5):1605–1611.
33. Deugnier Y, Turlin B. Pathology of hepatic iron overload. World J Gastroenterol 2007;13(35):4755–4760. [PubMed: 17729397]
34. Gordeuk VR, Bacon BR, Brittenham GM. Iron overload: causes and consequences. Annu Rev Nutr 1987;7:485–508. [PubMed: 3300744]
35. Gupta A, Baradaran H, Schweitzer AD, et al. Carotid plaque MRI and stroke risk: a systematic review and meta-analysis. Stroke 2013;44(11):3071–3077. [PubMed: 23988640]
36. Saam T, Hetterich H, Hoffmann V, et al. Meta-analysis and systematic review of the predictive value of carotid plaque hemorrhage on cerebrovascular events by magnetic resonance imaging. J Am Coll Cardiol 2013;62(12):1081–1091. [PubMed: 23850912]
37. Sickles EA. Breast calcifications: mammographic evaluation. Radiology 1986;160(2):289–293. [PubMed: 3726103]
38. Cao JJ, Huang W, Wu HS, Cao M, Zhang Y, Jin XD. Prostatic Calculi: Do They Matter? Sex Med Rev 2018;6(3):482–491. [PubMed: 29157875]
39. Bataller R, Brenner DA. Liver fibrosis. J Clin Invest 2005;115(2):209–218. [PubMed: 15690074]
40. Nguyen TD, Wen Y, Du J, et al. Quantitative susceptibility mapping of carotid plaques using nonlinear total field inversion: Initial experience in patients with significant carotid stenosis. Magn Reson Med 2020;84(3):1501–1509. [PubMed: 32141644]
41. Guo Y, Chen Y, Zhang X, et al. Magnetic Susceptibility and Fat Content in the Lumbar Spine of Postmenopausal Women With Varying Bone Mineral Density. J Magn Reson Imaging 2019;49(4):1020–1028. [PubMed: 30252983]

42. Guo Y, Liu Z, Wen Y, et al. Quantitative susceptibility mapping of the spine using in-phase echoes to initialize inhomogeneous field and R2* for the nonconvex optimization problem of fat-water separation. NMR Biomed 2019;32(11):e4156. [PubMed: 31424131]

43. Boehm C, Sollmann N, Meineke J, et al. Preconditioned water-fat total field inversion: Application to spine quantitative susceptibility mapping. Magn Reson Med 2022;87(1):417–430. [PubMed: 34255370]

44. Schweser K-HH F, Deistung A, Atterbury M, Baltzer PA, Burmeister HP, Kaiser WA, and Reichenbach JR Quantitative magnetic susceptibility mapping (QSM) in breast disease reveals additional information for MR-based characterization of carcinoma and calcification. Proc Intl Soc Mag Reson Med. Volume 19; 2011. p. 1014.

45. Wen Y, Nguyen TD, Liu Z, et al. Cardiac quantitative susceptibility mapping (QSM) for heart chamber oxygenation. Magn Reson Med 2018;79(3):1545–1552. [PubMed: 28653375]

46. Li J, Tak K, Meier R, et al. Quantitative Susceptibility Mapping for Chamber Blood Oxygenation in Pulmonary Hypertension: Validation using Right Heart Catheterization. Proceedings of the 2022 ISMRM & ISMRT Annual Meeting, London; program number 4449.

47. Straub S, Laun FB, Emmerich J, et al. Potential of quantitative susceptibility mapping for detection of prostatic calcifications. J Magn Reson Imaging 2017;45(3):889–898. [PubMed: 27418017]

48. Sharma SD, Fischer R, Schoennagel BP, et al. MRI-based quantitative susceptibility mapping (QSM) and R2* mapping of liver iron overload: Comparison with SQUID-based biomagnetic liver susceptometry. Magn Reson Med 2017;78(1):264–270. [PubMed: 27509836]

49. Sharma SD, Hernando D, Horng DE, Reeder SB. Quantitative susceptibility mapping in the abdomen as an imaging biomarker of hepatic iron overload. Magn Reson Med 2015;74(3):673–683. [PubMed: 25199788]

50. Zhao R, Velikina J, Reeder SB, Vasanawala S, Jeng M, Hernando D. Validation of liver quantitative susceptibility mapping across imaging parameters at 1.5 T and 3.0 T using SQUID susceptometry as reference. Magn Reson Med 2022.

51. Jafari R, Hectors SJ, Koehne de Gonzalez AK, et al. Integrated quantitative susceptibility and R(2) * mapping for evaluation of liver fibrosis: An ex vivo feasibility study. NMR Biomed 2021;34(1):e4412. [PubMed: 32959425]

52. Qu Z, Yang S, Xing F, et al. Magnetic resonance quantitative susceptibility mapping in the evaluation of hepatic fibrosis in chronic liver disease: a feasibility study. Quant Imaging Med Surg 2021;11(4):1170–1183. [PubMed: 33816158]

53. Bechler E, Stabinska J, Thiel T, et al. Feasibility of quantitative susceptibility mapping (QSM) of the human kidney. Magn Reson Mater Phy 2021;34(3):389–397.

54. Dymerska B, Bohndorf K, Schennach P, Rauscher A, Trattnig S, Robinson SD. In vivo phase imaging of human epiphyseal cartilage at 7 T. Magnetic Resonance in Medicine 2018;79(4):2149–2155. [PubMed: 28758241]

55. Wei H, Lin H, Qin L, et al. Quantitative susceptibility mapping of articular cartilage in patients with osteoarthritis at 3T. J Magn Reson Imaging 2019;49(6):1665–1675. [PubMed: 30584684]

56. Dimov AV, Liu Z, Spincemaille P, Prince MR, Du J, Wang Y. Bone quantitative susceptibility mapping using a chemical species-specific R2* signal model with ultrashort and conventional echo data. Magn Reson Med 2018;79(1):121–128. [PubMed: 28261863]

57. Yu H, Shimakawa A, McKenzie CA, Brodsky E, Brittain JH, Reeder SB. Multiecho water-fat separation and simultaneous R2* estimation with multifrequency fat spectrum modeling. Magn Reson Med 2008;60(5):1122–1134. [PubMed: 18956464]

58. Liu T, Wisnieff C, Lou M, Chen W, Spincemaille P, Wang Y. Nonlinear formulation of the magnetic field to source relationship for robust quantitative susceptibility mapping. Magn Reson Med 2013;69(2):467–476. [PubMed: 22488774]

59. Tsao J, Jiang Y. Hierarchical IDEAL: fast, robust, and multiresolution separation of multiple chemical species from multiple echo times. Magn Reson Med 2013;70(1):155–159. [PubMed: 22887356]

60. Zhong X, Nickel MD, Kannengiesser SA, Dale BM, Kiefer B, Bashir MR. Liver fat quantification using a multi-step adaptive fitting approach with multi-echo GRE imaging. Magn Reson Med 2014;72(5):1353–1365. [PubMed: 24323332]

61. Yu H, McKenzie CA, Shimakawa A, et al. Multiecho reconstruction for simultaneous water-fat decomposition and T2* estimation. J Magn Reson Imaging 2007;26(4):1153–1161. [PubMed: 17896369]
62. Reeder SB, Pineda AR, Wen Z, et al. Iterative decomposition of water and fat with echo asymmetry and least-squares estimation (IDEAL): application with fast spin-echo imaging. Magn Reson Med 2005;54(3):636–644. [PubMed: 16092103]
63. Yu H, Reeder SB, Shimakawa A, Brittain JH, Pelc NJ. Field map estimation with a region growing scheme for iterative 3-point water-fat decomposition. Magn Reson Med 2005;54(4):1032–1039. [PubMed: 16142718]
64. Reeder SB, Wen Z, Yu H, et al. Multicoil Dixon chemical species separation with an iterative least-squares estimation method. Magn Reson Med 2004;51(1):35–45. [PubMed: 14705043]
65. Lu W, Hargreaves BA. Multiresolution field map estimation using golden section search for water-fat separation. Magn Reson Med 2008;60(1):236–244. [PubMed: 18581397]
66. Yu H, Reeder SB, Shimakawa A, McKenzie CA, Brittain JH. Robust multipoint water-fat separation using fat likelihood analysis. Magn Reson Med 2012;67(4):1065–1076. [PubMed: 21842498]
67. Ma J Breath-hold water and fat imaging using a dual-echo two-point Dixon technique with an efficient and robust phase-correction algorithm. Magn Reson Med 2004;52(2):415–419. [PubMed: 15282827]
68. Ma JF. A single-point dixon technique for fat-suppressed fast 3D gradient-echo Imaging with a flexible echo time. Journal of Magnetic Resonance Imaging 2008;27(4):881–890. [PubMed: 18302201]
69. Berglund J, Johansson L, Ahlstrom H, Kullberg J. Three-point Dixon method enables whole-body water and fat imaging of obese subjects. Magn Reson Med 2010;63(6):1659–1668. [PubMed: 20512869]
70. Eggers H, Bornert P. Chemical Shift Encoding-Based Water-Fat Separation Methods. Journal of Magnetic Resonance Imaging 2014;40(2):251–268. [PubMed: 24446249]
71. Hernando D, Kellman P, Haldar JP, Liang ZP. Robust water/fat separation in the presence of large field inhomogeneities using a graph cut algorithm. Magn Reson Med 2010;63(1):79–90. [PubMed: 19859956]
72. Cui C, Shah A, Wu X, Jacob M. A rapid 3D fat-water decomposition method using globally optimal surface estimation (R-GOOSE). Magn Reson Med 2018;79(4):2401–2407. [PubMed: 28726301]
73. Cui C, Wu X, Newell JD, Jacob M. Fat water decomposition using globally optimal surface estimation (GOOSE) algorithm. Magn Reson Med 2015;73(3):1289–1299. [PubMed: 24604689]
74. Dong J, Liu T, Chen F, et al. Simultaneous phase unwrapping and removal of chemical shift (SPURS) using graph cuts: application in quantitative susceptibility mapping. IEEE Trans Med Imaging 2015;34(2):531–540. [PubMed: 25312917]
75. Berglund J, Kullberg J. Three-dimensional water/fat separation and T2* estimation based on whole-image optimization--application in breathhold liver imaging at 1.5 T. Magn Reson Med 2012;67(6):1684–1693. [PubMed: 22189760]
76. Stinson EG, Trzasko JD, Fletcher JG, Riederer SJ. Dual echo Dixon imaging with a constrained phase signal model and graph cuts reconstruction. Magn Reson Med 2017;78(6):2203–2215. [PubMed: 28150873]
77. Berglund J, Skorpil M. Multi-scale graph-cut algorithm for efficient water-fat separation. Magn Reson Med 2017;78(3):941–949. [PubMed: 27714826]
78. Jafari R, Sheth S, Spincemaille P, et al. Rapid automated liver quantitative susceptibility mapping. J Magn Reson Imaging 2019;50(3):725–732. [PubMed: 30637892]
79. Goldfarb JW, Craft J, Cao JJ. Water-fat separation and parameter mapping in cardiac MRI via deep learning with a convolutional neural network. J Magn Reson Imaging 2019;50(2):655–665. [PubMed: 30701621]
80. Andersson J, Ahlstrom H, Kullberg J. Separation of water and fat signal in whole-body gradient echo scans using convolutional neural networks. Magn Reson Med 2019;82(3):1177–1186. [PubMed: 31033022]

81. Jafari R, Spincemaille P, Zhang J, et al. Deep neural network for water/fat separation: Supervised training, unsupervised training, and no training. Magn Reson Med 2021;85(4):2263–2277. [PubMed: 33107127]

82. Liu K, Li X, Li Z, et al. Robust water-fat separation based on deep learning model exploring multi-echo nature of mGRE. Magn Reson Med 2021;85(5):2828–2841. [PubMed: 33231896]

83. Chen X, Wang W, Huang J, et al. Ultrafast water-fat separation using deep learning-based single-shot MRI. Magn Reson Med 2022;87(6):2811–2825. [PubMed: 35099082]

84. Wu Y, Alley M, Li Z, et al. Deep Learning-Based Water-Fat Separation from Dual-Echo Chemical Shift-Encoded Imaging. Bioengineering (Basel) 2022;9(10).

85. Hanspach J, Bollmann S, Grigo J, Karius A, Uder M, Laun FB. Deep learning-based quantitative susceptibility mapping (QSM) in the presence of fat using synthetically generated multi-echo phase training data. Magn Reson Med 2022;88(4):1548–1560. [PubMed: 35713187]

86. Bechler E, Stabinska J, Thiel T, et al. Feasibility of quantitative susceptibility mapping (QSM) of the human kidney. MAGMA 2021;34(3):389–397. [PubMed: 33230656]

87. Sato R, Shirai T, Soutome Y, Bito Y, Ochi H. Quantitative susceptibility mapping of prostate with separate calculations for water and fat regions for reducing shading artifacts. Magn Reson Imaging 2020;66:22–29. [PubMed: 31715250]

88. Jerban S, Lu X, Jang H, et al. Significant correlations between human cortical bone mineral density and quantitative susceptibility mapping (QSM) obtained with 3D Cones ultrashort echo time magnetic resonance imaging (UTE-MRI). Magn Reson Imaging 2019;62:104–110. [PubMed: 31247253]

89. Jang H, von Drygalski A, Wong J, et al. Ultrashort echo time quantitative susceptibility mapping (UTE-QSM) for detection of hemosiderin deposition in hemophilic arthropathy: A feasibility study. Magn Reson Med 2020;84(6):3246–3255. [PubMed: 32662904]

90. Li J, Nguyen TD, Kim J, Wang Y, Weinsaft JW, Spincemaille P. Accelerated Stack-of-Spiral Data Acquisition for Cardiac Quantitative Susceptibility Mapping. Proceedings of the 2022 Joint Workshop on MR phase, magnetic susceptibility and electrical properties mapping, Lucca.

91. Wang Y, Rossman PJ, Grimm RC, Riederer SJ, Ehman RL. Navigator-echo-base real-time respiratory gating and triggering for reduction of respiration effects in three-dimensional coronary MR angiography. Radiology 1996;198(1):55–60. [PubMed: 8539406]

92. Li DB, Kaushikkar S, Haacke EM, et al. Coronary arteries: Three-dimensional MR imaging with retrospective respiratory gating. Radiology 1996;201(3):857–863. [PubMed: 8939242]

93. Ahn CB, Kim JH, Cho ZH. High-speed spiral-scan echo planar NMR imaging-I. IEEE Trans Med Imaging 1986;5(1):2–7. [PubMed: 18243976]

94. Delattre BM, Heidemann RM, Crowe LA, Vallee JP, Hyacinthe JN. Spiral demystified. Magn Reson Imaging 2010;28(6):862–881. [PubMed: 20409660]

95. Kang M, Jafari R, Behr GG, Otazo R, Kee Y. Free-Breathing Liver QSM with High Isotropic Resolution Using Respiratory Motion-Resolved 3D Multi-Echo Cones MRI. Proceedings of the 2022 ISMRM & ISMRT Annual Meeting, London; program number 0116.

96. Hollingsworth KG. Reducing acquisition time in clinical MRI by data undersampling and compressed sensing reconstruction. Phys Med Biol 2015;60(21):R297–322. [PubMed: 26448064]

97. Man LC, Pauly JM, Macovski A. Multifrequency interpolation for fast off-resonance correction. Magn Reson Med 1997;37(5):785–792. [PubMed: 9126954]

98. Brodsky EK, Holmes JH, Yu H, Reeder SB. Generalized k-space decomposition with chemical shift correction for non-Cartesian water-fat imaging. Magn Reson Med 2008;59(5):1151–1164. [PubMed: 18429018]

99. Wu B, Li W, Avram AV, Gho SM, Liu C. Fast and tissue-optimized mapping of magnetic susceptibility and T2* with multi-echo and multi-shot spirals. Neuroimage 2012;59(1):297–305. [PubMed: 21784162]

100. Karsa A, Punwani S, Shmueli K. An optimized and highly repeatable MRI acquisition and processing pipeline for quantitative susceptibility mapping in the head-and-neck region. Magn Reson Med 2020;84(6):3206–3222. [PubMed: 32621302]

101. Li J, Lin H, Liu T, et al. Quantitative susceptibility mapping (QSM) minimizes interference from cellular pathology in R2* estimation of liver iron concentration. J Magn Reson Imaging 2018;48(4):1069–1079. [PubMed: 29566449]

102. Xu B, Liu T, Spincemaille P, Prince M, Wang Y. Flow compensated quantitative susceptibility mapping for venous oxygenation imaging. Magn Reson Med 2014;72(2):438–445. [PubMed: 24006187]

103. Liu T, Khalidov I, de Rochefort L, et al. A novel background field removal method for MRI using projection onto dipole fields (PDF). NMR Biomed 2011;24(9):1129–1136. [PubMed: 21387445]

104. Zhou D, Liu T, Spincemaille P, Wang Y. Background field removal by solving the Laplacian boundary value problem. NMR Biomed 2014;27(3):312–319. [PubMed: 24395595]

105. Fang J, Bao L, Li X, van Zijl PCM, Chen Z. Background field removal using a region adaptive kernel for quantitative susceptibility mapping of human brain. J Magn Reson 2017;281:130–140. [PubMed: 28595120]

106. Kan H, Kasai H, Arai N, Kunitomo H, Hirose Y, Shibamoto Y. Background field removal technique using regularization enabled sophisticated harmonic artifact reduction for phase data with varying kernel sizes. Magn Reson Imaging 2016;34(7):1026–1033. [PubMed: 27114339]

107. Schweser F, Robinson SD, de Rochefort L, Li W, Bredies K. An illustrated comparison of processing methods for phase MRI and QSM: removal of background field contributions from sources outside the region of interest. NMR Biomed 2017;30(4).

108. Li W, Avram AV, Wu B, Xiao X, Liu CL. Integrated Laplacian-based phase unwrapping and background phase removal for quantitative susceptibility mapping. NMR in Biomedicine 2014;27(2):219–227. [PubMed: 24357120]

109. Kee Y, Liu Z, Zhou L, et al. Quantitative Susceptibility Mapping (QSM) Algorithms: Mathematical Rationale and Computational Implementations. IEEE Trans Biomed Eng 2017;64(11):2531–2545. [PubMed: 28885147]

110. Wei H, Dibb R, Zhou Y, et al. Streaking artifact reduction for quantitative susceptibility mapping of sources with large dynamic range. NMR Biomed 2015;28(10):1294–1303. [PubMed: 26313885]

111. Buch S, Liu S, Ye Y, Cheng YC, Neelavalli J, Haacke EM. Susceptibility mapping of air, bone, and calcium in the head. Magn Reson Med 2015;73(6):2185–2194. [PubMed: 25046134]

112. Straub S, Emmerich J, Schlemmer HP, et al. Mask-Adapted Background Field Removal for Artifact Reduction in Quantitative Susceptibility Mapping of the Prostate. Tomography 2017;3(2):96–100. [PubMed: 30042974]

113. Sun H, Kate M, Gioia LC, Emery DJ, Butcher K, Wilman AH. Quantitative susceptibility mapping using a superposed dipole inversion method: Application to intracranial hemorrhage. Magn Reson Med 2016;76(3):781–791. [PubMed: 26414757]

114. Zun Z, Kapse K, Quistorff J, et al. Feasibility of QSM in the human placenta. Magn Reson Med 2021;85(3):1272–1281. [PubMed: 32936489]

115. Liu Z, Kee Y, Zhou D, Wang Y, Spincemaille P. Preconditioned total field inversion (TFI) method for quantitative susceptibility mapping. Magn Reson Med 2017;78(1):303–315. [PubMed: 27464893]

116. Wen Y, Spincemaille P, Nguyen T, et al. Multiecho complex total field inversion method (mcTFI) for improved signal modeling in quantitative susceptibility mapping. Magn Reson Med 2021;86(4):2165–2178. [PubMed: 34028868]

117. Brittenham GM, Badman DG, National Institute of D, Digestive, Kidney Diseases W. Noninvasive measurement of iron: report of an NIDDK workshop. Blood 2003;101(1):15–19. [PubMed: 12393526]

118. Philippe MA, Ruddell RG, Ramm GA. Role of iron in hepatic fibrosis: one piece in the puzzle. World J Gastroenterol 2007;13(35):4746–4754. [PubMed: 17729396]

119. Pietrangelo A. Iron and the liver. Liver Int 2016;36 Suppl 1:116–123. [PubMed: 26725908]

120. Mobarra N, Shanaki M, Ehteram H, et al. A Review on Iron Chelators in Treatment of Iron Overload Syndromes. Int J Hematol Oncol Stem Cell Res 2016;10(4):239–247. [PubMed: 27928480]

121. Poggiali E, Cassinerio E, Zanaboni L, Cappellini MD. An update on iron chelation therapy. Blood Transfus 2012;10(4):411–422. [PubMed: 22790257]

122. Porter JB. Practical management of iron overload. Br J Haematol 2001;115(2):239–252. [PubMed: 11703317]

123. Lin H, Wei H, He N, et al. Quantitative susceptibility mapping in combination with water-fat separation for simultaneous liver iron and fat fraction quantification. Eur Radiol 2018;28(8):3494–3504. [PubMed: 29470640]

124. Krafft AJ, Loeffler RB, Song R, et al. Quantitative ultrashort echo time imaging for assessment of massive iron overload at 1.5 and 3 Tesla. Magn Reson Med 2017;78(5):1839–1851. [PubMed: 28090666]

125. Wen Y, Weinsaft JW, Nguyen TD, et al. Free breathing three-dimensional cardiac quantitative susceptibility mapping for differential cardiac chamber blood oxygenation - initial validation in patients with cardiovascular disease inclusive of direct comparison to invasive catheterization. J Cardiovasc Magn Reson 2019;21(1):70. [PubMed: 31735165]

126. Sandoval J, Bauerle O, Palomar A, et al. Survival in primary pulmonary hypertension. Validation of a prognostic equation. Circulation 1994;89(4):1733–1744. [PubMed: 8149539]

127. Swiston JR, Johnson SR, Granton JT. Factors that prognosticate mortality in idiopathic pulmonary arterial hypertension: a systematic review of the literature. Respir Med 2010;104(11):1588–1607. [PubMed: 20810261]

128. Gallet R, Lellouche N, Mitchell-Heggs L, et al. Prognosis value of central venous oxygen saturation in acute decompensated heart failure. Arch Cardiovasc Dis 2012;105(1):5–12. [PubMed: 22369912]

129. Mullens W, Abrahams Z, Skouri HN, et al. Prognostic evaluation of ambulatory patients with advanced heart failure. Am J Cardiol 2008;101(9):1297–1302. [PubMed: 18435961]

130. Patel CB, DeVore AD, Felker GM, et al. Characteristics and outcomes of patients with heart failure and discordant findings by right-sided heart catheterization and cardiopulmonary exercise testing. Am J Cardiol 2014;114(7):1059–1064. [PubMed: 25212547]

131. Judge O, Ji F, Fleming N, Liu H. Current use of the pulmonary artery catheter in cardiac surgery: a survey study. J Cardiothorac Vasc Anesth 2015;29(1):69–75. [PubMed: 25440650]

132. Brovman EY, Gabriel RA, Dutton RP, Urman RD. Pulmonary Artery Catheter Use During Cardiac Surgery in the United States, 2010 to 2014. J Cardiothorac Vasc Anesth 2016;30(3):579–584. [PubMed: 26947712]

133. Fernandez-Seara MA, Techawiboonwong A, Detre JA, Wehrli FW. MR susceptometry for measuring global brain oxygen extraction. Magn Reson Med 2006;55(5):967–973. [PubMed: 16598726]

134. Wright GA, Hu BS, Macovski A. Estimating oxygen saturation of blood in vivo with MR imaging at 1.5 T. Journal of Magnetic Resonance Imaging 1991;1(3):275–283. [PubMed: 1802140]

135. Li D, Wang Y, Waight DJ. Blood oxygen saturation assessment in vivo using T2 * estimation. Magnetic Resonance in Medicine 1998;39(5):685–690. [PubMed: 9581597]

136. Silvennoinen MJ, Kettunen MI, Kauppinen RA. Effects of hematocrit and oxygen saturation level on blood spin-lattice relaxation. Magnetic Resonance in Medicine 2003;49(3):568–571. [PubMed: 12594761]

137. Lu H, Ge Y. Quantitative evaluation of oxygenation in venous vessels using T2-Relaxation-Under-Spin-Tagging MRI. Magnetic Resonance in Medicine 2008;60(2):357–363. [PubMed: 18666116]

138. Thulborn KR, Waterton JC, Matthews PM, Radda GK. Oxygenation dependence of the transverse relaxation time of water protons in whole blood at high field. Biochimica et Biophysica Acta (BBA) - General Subjects 1982;714(2):265–270. [PubMed: 6275909]

139. Ogawa S, Menon RS, Tank DW, et al. Functional brain mapping by blood oxygenation level-dependent contrast magnetic resonance imaging. A comparison of signal characteristics with a biophysical model. Biophysical journal 1993;64(3):803–812. [PubMed: 8386018]

140. Golay X, Silvennoinen MJ, Zhou J, et al. Measurement of tissue oxygen extraction ratios from venous blood T2: Increased precision and validation of principle. Magnetic Resonance in Medicine 2001;46(2):282–291. [PubMed: 11477631]

141. Bolar DS, Rosen BR, Sorensen AG, Adalsteinsson E. QUantitative Imaging of eXtraction of oxygen and TIssue consumption (QUIXOTIC) using venular-targeted velocity-selective spin labeling. Magnetic Resonance in Medicine 2011;66(6):1550–1562. [PubMed: 21674615]

142. Yablonskiy DA, Sukstanskii AL, He X. Blood oxygenation level-dependent (BOLD)-based techniques for the quantification of brain hemodynamic and metabolic properties - theoretical models and experimental approaches. NMR Biomed 2013;26(8):963–986. [PubMed: 22927123]

143. Varghese J, Potter LC, LaFountain R, et al. CMR-based blood oximetry via multi-parametric estimation using multiple T2 measurements. Journal of Cardiovascular Magnetic Resonance 2017;19(1):88. [PubMed: 29121971]

144. Varghese J, Smyke M, Pan Y, et al. Patient-Adaptive Magnetic Resonance Oximetry: Comparison With Invasive Catheter Measurement of Blood Oxygen Saturation in Patients With Cardiovascular Disease. J Magn Reson Imaging 2020;52(5):1449–1459. [PubMed: 32356905]

145. Liu Z, Spincemaille P, Yao Y, Zhang Y, Wang Y. MEDI+0: Morphology enabled dipole inversion with automatic uniform cerebrospinal fluid zero reference for quantitative susceptibility mapping. Magn Reson Med 2018;79(5):2795–2803. [PubMed: 29023982]

146. Abramowitz Y, Jilaihawi H, Chakravarty T, Mack MJ, Makkar RR. Mitral Annulus Calcification. J Am Coll Cardiol 2015;66(17):1934–1941. [PubMed: 26493666]

147. Guerrero M, Wang DD, Pursnani A, et al. A Cardiac Computed Tomography-Based Score to Categorize Mitral Annular Calcification Severity and Predict Valve Embolization. JACC Cardiovasc Imaging 2020;13(9):1945–1957. [PubMed: 32417332]

148. Schenck JF. The role of magnetic susceptibility in magnetic resonance imaging: MRI magnetic compatibility of the first and second kinds. Med Phys 1996;23(6):815–850. [PubMed: 8798169]

149. Li J, Mitlak H, Nambiar L, et al. Quantitative Susceptibility Mapping for Mitral Annulus Calcification Detection via Validation of Computed Tomography/Echocardiography. ISMRM May 2021, Paris, France (Virtual) p 3622 2021.

150. Moon BF, Iyer SK, Hwuang E, et al. Iron imaging in myocardial infarction reperfusion injury. Nat Commun 2020;11(1):3273. [PubMed: 32601301]

151. Flaherty ML, Kissela B, Khoury JC, et al. Carotid artery stenosis as a cause of stroke. Neuroepidemiology 2013;40(1):36–41. [PubMed: 23075828]

152. Barnett HJ, Taylor DW, Eliasziw M, et al. Benefit of carotid endarterectomy in patients with symptomatic moderate or severe stenosis. North American Symptomatic Carotid Endarterectomy Trial Collaborators. N Engl J Med 1998;339(20):1415–1425. [PubMed: 9811916]

153. Randomised trial of endarterectomy for recently symptomatic carotid stenosis: final results of the MRC European Carotid Surgery Trial (ECST). Lancet 1998;351(9113):1379–1387. [PubMed: 9593407]

154. Rothwell PM, Gutnikov SA, Warlow CP, European Carotid Surgery Trialist’s C. Reanalysis of the final results of the European Carotid Surgery Trial. Stroke 2003;34(2):514–523. [PubMed: 12574569]

155. Kamel H, Navi BB, Merkler AE, et al. Reclassification of Ischemic Stroke Etiological Subtypes on the Basis of High-Risk Nonstenosing Carotid Plaque. Stroke 2020;51(2):504–510. [PubMed: 31847749]

156. Singh N, Marko M, Ospel JM, Goyal M, Almekhlafi M. The Risk of Stroke and TIA in Nonstenotic Carotid Plaques: A Systematic Review and Meta-Analysis. AJNR Am J Neuroradiol 2020;41(8):1453–1459. [PubMed: 32646945]

157. Schindler A, Schinner R, Altaf N, et al. Prediction of Stroke Risk by Detection of Hemorrhage in Carotid Plaques: Meta-Analysis of Individual Patient Data. JACC Cardiovasc Imaging 2020;13(2 Pt 1):395–406. [PubMed: 31202755]

158. Baradaran H, Al-Dasuqi K, Knight-Greenfield A, et al. Association between Carotid Plaque Features on CTA and Cerebrovascular Ischemia: A Systematic Review and Meta-Analysis. Am J Neuroradiol 2017;38(12):2321–2326. [PubMed: 29074638]

159. Yuan C, Mitsumori LM, Ferguson MS, et al. In vivo accuracy of multispectral magnetic resonance imaging for identifying lipid-rich necrotic cores and intraplaque hemorrhage in advanced human carotid plaques. Circulation 2001;104(17):2051–2056. [PubMed: 11673345]

160. Saam T, Ferguson MS, Yarnykh VL, et al. Quantitative evaluation of carotid plaque composition by in vivo MRI. Arterioscler Thromb Vasc Biol 2005;25(1):234–239. [PubMed: 15528475]

161. Cai JM, Hatsukami TS, Ferguson MS, Small R, Polissar NL, Yuan C. Classification of human carotid atherosclerotic lesions with in vivo multicontrast magnetic resonance imaging. Circulation 2002;106(11):1368–1373. [PubMed: 12221054]

162. Saba L, Yuan C, Hatsukami TS, et al. Carotid Artery Wall Imaging: Perspective and Guidelines from the ASNR Vessel Wall Imaging Study Group and Expert Consensus Recommendations of the American Society of Neuroradiology. AJNR Am J Neuroradiol 2018;39(2):E9–E31. [PubMed: 29326139]

163. Chu B, Kampschulte A, Ferguson MS, et al. Hemorrhage in the atherosclerotic carotid plaque: a high-resolution MRI study. Stroke 2004;35(5):1079–1084. [PubMed: 15060318]

164. Bradley WG Jr. MR appearance of hemorrhage in the brain. Radiology 1993;189(1):15–26. [PubMed: 8372185]

165. Underhill HR, Yarnykh VL, Hatsukami TS, et al. Carotid plaque morphology and composition: initial comparison between 1.5- and 3.0-T magnetic field strengths. Radiology 2008;248(2):550–560. [PubMed: 18574135]

166. Chen W, Zhu W, Kovanlikaya I, et al. Intracranial calcifications and hemorrhages: characterization with quantitative susceptibility mapping. Radiology 2014;270(2):496–505. [PubMed: 24126366]

167. Ikebe Y, Ishimaru H, Imai H, et al. Quantitative Susceptibility Mapping for Carotid Atherosclerotic Plaques: A Pilot Study. Magn Reson Med Sci 2020;19(2):135–140. [PubMed: 31155568]

168. Azuma M, Maekawa K, Yamashita A, et al. Characterization of Carotid Plaque Components by Quantitative Susceptibility Mapping. Am J Neuroradiol 2020;41(2):310–317. [PubMed: 31879331]

169. Wang C, Zhang Y, Du J, et al. Quantitative Susceptibility Mapping for Characterization of Intraplaque Hemorrhage and Calcification in Carotid Atherosclerotic Disease. J Magn Reson Imaging 2020;52(2):534–541. [PubMed: 32039515]

170. Ruetten PPR, Cluroe AD, Usman A, Priest AN, Gillard JH, Graves MJ. Simultaneous MRI water-fat separation and quantitative susceptibility mapping of carotid artery plaque pre- and post-ultrasmall superparamagnetic iron oxide-uptake. Magn Reson Med 2020;84(2):686–697. [PubMed: 31961969]

171. Bachrata B, Strasser B, Bogner W, et al. Simultaneous Multiple Resonance Frequency imaging (SMURF): Fat-water imaging using multi-band principles. Magn Reson Med 2021;85(3):1379–1396. [PubMed: 32981114]

172. Bachrata B, Trattnig S, Robinson SD. Quantitative susceptibility mapping of the head-and-neck using SMURF fat-water imaging with chemical shift and relaxation rate corrections. Magn Reson Med 2022;87(3):1461–1479. [PubMed: 34850446]

173. Zhou Z, Li R, Zhao X, et al. Evaluation of 3D multi-contrast joint intra- and extracranial vessel wall cardiovascular magnetic resonance. J Cardiovasc Magn Reson 2015;17(1):41. [PubMed: 26013973]

174. Shin HG, Lee J, Yun YH, et al. chi-separation: Magnetic susceptibility source separation toward iron and myelin mapping in the brain. Neuroimage 2021;240:118371. [PubMed: 34242783]

175. Dimov AV, Nguyen TD, Gillen KM, et al. Susceptibility source separation from gradient echo data using magnitude decay modeling. J Neuroimaging 2022;32(5):852–859. [PubMed: 35668022]

176. Chen J, Gong NJ, Chaim KT, Otaduy MCG, Liu C. Decompose quantitative susceptibility mapping (QSM) to sub-voxel diamagnetic and paramagnetic components based on gradient-echo MRI data. Neuroimage 2021;242:118477. [PubMed: 34403742]

177. Emmerich J, Bachert P, Ladd ME, Straub S. On the separation of susceptibility sources in quantitative susceptibility mapping: Theory and phantom validation with an in vivo application to multiple sclerosis lesions of different age. J Magn Reson 2021;330:107033. [PubMed: 34303117]

178. Cao T, Ma S, Wang N, et al. Three-dimensional simultaneous brain mapping of T1, T2, T2 * and magnetic susceptibility with MR Multitasking. Magn Reson Med 2022;87(3):1375–1389. [PubMed: 34708438]

179. Caan MWA, Bazin PL, Marques JP, de Hollander G, Dumoulin SO, van der Zwaag W. MP2RAGEME: T(1), T(2)(*), and QSM mapping in one sequence at 7 tesla. Hum Brain Mapp 2019;40(6):1786–1798. [PubMed: 30549128]

180. Sun H, Cleary JO, Glarin R, et al. Extracting more for less: multi-echo MP2RAGE for simultaneous T(1)-weighted imaging, T(1) mapping, R2 * mapping, SWI, and QSM from a single acquisition. Magn Reson Med 2020;83(4):1178–1191. [PubMed: 31502729]

181. Nissi MJ, Toth F, Wang L, Carlson CS, Ellermann JM. Improved Visualization of Cartilage Canals Using Quantitative Susceptibility Mapping. PLoS One 2015;10(7):e0132167. [PubMed: 26168296]

182. Wei H, Gibbs E, Zhao P, et al. Susceptibility tensor imaging and tractography of collagen fibrils in the articular cartilage. Magn Reson Med 2017;78(5):1683–1690. [PubMed: 28856712]

183. Wei H, Dibb R, Decker K, et al. Investigating magnetic susceptibility of human knee joint at 7 Tesla. Magn Reson Med 2017;78(5):1933–1943. [PubMed: 28097689]

184. Zhang M, Li Y, Feng R, et al. Change in Susceptibility Values in Knee Cartilage After Marathon Running Measured Using Quantitative Susceptibility Mapping. J Magn Reson Imaging 2021;54(5):1585–1593. [PubMed: 34031930]

185. Wang LN, Nissi MJ, Toth F, et al. Quantitative Susceptibility Mapping Detects Abnormalities in Cartilage Canals in a Goat Model of Preclinical Osteochondritis Dissecans. Magnetic Resonance in Medicine 2017;77(3):1276–1283. [PubMed: 27018370]

186. Nykanen O, Rieppo L, Toyras J, et al. Quantitative susceptibility mapping of articular cartilage: Ex vivo findings at multiple orientations and following different degradation treatments. Magn Reson Med 2018;80(6):2702–2716. [PubMed: 29687923]

187. Nykanen O, Sarin JK, Ketola JH, et al. T2* and quantitative susceptibility mapping in an equine model of post-traumatic osteoarthritis: assessment of mechanical and structural properties of articular cartilage. Osteoarthritis Cartilage 2019;27(10):1481–1490. [PubMed: 31276818]

188. Zhang M, Li Z, Wang H, et al. Simultaneous Quantitative Susceptibility Mapping of Articular Cartilage and Cortical Bone of Human Knee Joint Using Ultrashort Echo Time Sequences. Front Endocrinol (Lausanne) 2022;13:844351. [PubMed: 35273576]

189. Glyn-Jones S, Palmer AJ, Agricola R, et al. Osteoarthritis. Lancet 2015;386(9991):376–387. [PubMed: 25748615]

190. Hellio Le Graverand MP, Sciore P, Eggerer J, et al. Formation and phenotype of cell clusters in osteoarthritic meniscus. Arthritis Rheum 2001;44(8):1808–1818. [PubMed: 11508433]

191. Fukui N, Purple CR, Sandell LJ. Cell biology of osteoarthritis: the chondrocyte's response to injury. Curr Rheumatol Rep 2001;3(6):496–505. [PubMed: 11709112]

192. Simon LS. Osteoarthritis: a review. Clin Cornerstone 1999;2(2):26–37. [PubMed: 10689542]

193. Arden N, Nevitt MC. Osteoarthritis: epidemiology. Best Pract Res Clin Rheumatol 2006;20(1):3–25. [PubMed: 16483904]

194. Hamerman D. The biology of osteoarthritis. N Engl J Med 1989;320(20):1322–1330. [PubMed: 2654632]

195. Oei EH, van Tiel J, Robinson WH, Gold GE. Quantitative radiologic imaging techniques for articular cartilage composition: toward early diagnosis and development of disease-modifying therapeutics for osteoarthritis. Arthritis Care Res (Hoboken) 2014;66(8):1129–1141. [PubMed: 24578345]

196. Compston JE, McClung MR, Leslie WD. Osteoporosis. Lancet 2019;393(10169):364–376. [PubMed: 30696576]

197. Eriksen EF. Cellular mechanisms of bone remodeling. Rev Endocr Metab Disord 2010;11(4):219–227. [PubMed: 21188536]

198. Hadjidakis DJ, Androulakis, II. Bone remodeling. Ann N Y Acad Sci 2006;1092:385–396. [PubMed: 17308163]

199. Bonnick SL. Osteoporosis in men and women. Clin Cornerstone 2006;8(1):28–39. [PubMed: 17591574]

200. Link TM. Radiology of Osteoporosis. Can Assoc Radiol J 2016;67(1):28–40. [PubMed: 26105503]

201. Hwang SN, Wehrli FW. The Calculation of the Susceptibility-Induced Magnetic-Field from 3D NMR Images with Applications to Trabecular Bone. J Magn Reson Ser B 1995;109(2):126–145.

202. Hopkins JA, Wehrli FW. Magnetic susceptibility measurement of insoluble solids by NMR: magnetic susceptibility of bone. Magn Reson Med 1997;37(4):494–500. [PubMed: 9094070]

203. Du J, Hermida JC, Diaz E, et al. Assessment of cortical bone with clinical and ultrashort echo time sequences. Magn Reson Med 2013;70(3):697–704. [PubMed: 23001864]

204. Murata N, Gonzalez-Cuyar LF, Murata K, et al. Macrocyclic and Other Non-Group 1 Gadolinium Contrast Agents Deposit Low Levels of Gadolinium in Brain and Bone Tissue: Preliminary Results From 9 Patients With Normal Renal Function. Invest Radiol 2016;51(7):447–453. [PubMed: 26863577]

205. Thakral C, Alhariri J, Abraham JL. Long-term retention of gadolinium in tissues from nephrogenic systemic fibrosis patient after multiple gadolinium-enhanced MRI scans: case report and implications. Contrast Media Mol Imaging 2007;2(4):199–205. [PubMed: 17712863]

206. Zhang X, Jang H, Chen Y, et al. Evaluation of Gadolinium Deposition in Cortical Bone Using 3D-UTE-QSM in vitro: Preliminary Study. Proceedings of the 2020 ISMRM & ISMRT Annual Meeting; program number 2781.

207. Sollmann N, Loffler MT, Kronthaler S, et al. MRI-Based Quantitative Osteoporosis Imaging at the Spine and Femur. Journal of Magnetic Resonance Imaging 2021;54(1):12–35. [PubMed: 32584496]

208. Boehm C, Diefenbach MN, Makowski MR, Karampinos DC. Improved body quantitative susceptibility mapping by using a variable-layer single-min-cut graph-cut for field-mapping. Magn Reson Med 2021;85(3):1697–1712. [PubMed: 33151604]

209. Siegel RL, Miller KD, Fuchs HE, Jemal A. Cancer statistics, 2022. CA Cancer J Clin 2022;72(1):7–33. [PubMed: 35020204]

210. Chin J, Rumble RB, Kollmeier M, et al. Brachytherapy for Patients With Prostate Cancer: American Society of Clinical Oncology/Cancer Care Ontario Joint Guideline Update. J Clin Oncol 2017;35(15):1737–1743. [PubMed: 28346805]

211. Maspero M, Seevinck PR, Willems NJW, et al. Evaluation of gold fiducial marker manual localisation for magnetic resonance-only prostate radiotherapy. Radiat Oncol 2018;13(1):105. [PubMed: 29871656]

212. Kao J, Karwowski P, Pettit J, Barney AK, Atalla C. Multiparametric prostate MRI-based intensity-modulated radiation therapy guided by prostatic calcifications. Br J Radiol 2020;93(1116):20200571. [PubMed: 32846099]

213. Nosrati R, Soliman A, Safigholi H, et al. MRI-based automated detection of implanted low dose rate (LDR) brachytherapy seeds using quantitative susceptibility mapping (QSM) and unsupervised machine learning (ML). Radiother Oncol 2018;129(3):540–547. [PubMed: 30243670]

214. Suh JH, Gardner JM, Kee KH, Shen S, Ayala AG, Ro JY. Calcifications in prostate and ejaculatory system: a study on 298 consecutive whole mount sections of prostate from radical prostatectomy or cystoprostatectomy specimens. Ann Diagn Pathol 2008;12(3):165–170. [PubMed: 18486891]

215. Ashley Wilton Stewart JG, Robinson Simon Daniel, O'Brien Kieran, Jin Jin, Barth Markus, and Bollmann Steffen. Quantitative Susceptibility Mapping as an Alternative to CT for Localizing Gold Intraprostatic Fiducial Markers. Proc Intl Soc Mag Reson Med 2022;30:3678.

216. Straub S, Laun FB, Emmerich J, et al. Potential of Quantitative Susceptibility Mapping for Detection of Prostatic Calcifications. J Magn Reson Imaging 2017;45(3):889–898. [PubMed: 27418017]

217. Sato R, Shirai T, Soutome Y, Bito Y, Ochi H. Quantitative susceptibility mapping of prostate with separate calculations for water and fat regions for reducing shading artifacts. Magn Reson Imaging 2020;66:22–29. [PubMed: 31715250]

218. Wang Y, Liu T. Quantitative Susceptibility Mapping (QSM): Decoding MRI Data for a Tissue Magnetic Biomarker. Magn Reson Med 2015;73(1):82–101. [PubMed: 25044035]

219. Bhattacharya M, Das A. Identification of tiny and large calcification in breast: a study on mammographic image analysis. Int J Bioinform Res Appl 2010;6(4):418–434. [PubMed: 20940127]

220. Dimov AV, Liu T, Spincemaille P, et al. Joint estimation of chemical shift and quantitative susceptibility mapping (chemical QSM). Magn Reson Med 2015;73(6):2100–2110. [PubMed: 24947227]

221. Christof Boehm JKS, Meineke Jakob, Ruschke Stefan, Weiss Kilian, Wu Mingming, Borde Tabea, Makowski Marcus R., Fallenberg Eva M., and Karampinos Dimitrios C. Mammography-like MR images using a preconditioned water-fat-silicone total field inversion QSM algorithm. Proc Intl Soc Mag Reson Med. Volume 30; 2022. p. 1588.

222. Li W, Liu C, Duong TQ, van Zijl PC, Li X. Susceptibility tensor imaging (STI) of the brain. NMR Biomed 2017;30(4).

223. Xie L, Dibb R, Cofer GP, et al. Susceptibility tensor imaging of the kidney and its microstructural underpinnings. Magn Reson Med 2015;73(3):1270–1281. [PubMed: 24700637]

224. Selby NM, Blankestijn PJ, Boor P, et al. Magnetic resonance imaging biomarkers for chronic kidney disease: a position paper from the European Cooperation in Science and Technology Action PARENCHIMA. Nephrol Dial Transplant 2018;33(suppl_2):ii4–ii14. [PubMed: 30137584]

225. Xie L, Sparks MA, Li W, et al. Quantitative susceptibility mapping of kidney inflammation and fibrosis in type 1 angiotensin receptor-deficient mice. NMR Biomed 2013;26(12):1853–1863. [PubMed: 24154952]

226. Xue C, Zhou C, Mei C. Total kidney volume: the most valuable predictor of autosomal dominant polycystic kidney disease progression. Kidney Int 2018;93(3):540–542. [PubMed: 29475545]

227. Higashihara E, Yamamoto K, Kaname S, et al. Age- and height-adjusted total kidney volume growth rate in autosomal dominant polycystic kidney diseases. Clin Exp Nephrol 2019;23(1):100–111. [PubMed: 30097754]

228. Chapman AB, Bost JE, Torres VE, et al. Kidney volume and functional outcomes in autosomal dominant polycystic kidney disease. Clin J Am Soc Nephrol 2012;7(3):479–486. [PubMed: 22344503]

229. Cornec-Le Gall E, Audrezet MP, Rousseau A, et al. The PROPKD Score: A New Algorithm to Predict Renal Survival in Autosomal Dominant Polycystic Kidney Disease. J Am Soc Nephrol 2016;27(3):942–951. [PubMed: 26150605]

230. Riyahi S, Dev H, Blumenfeld JD, et al. Hemorrhagic Cysts and Other MR Biomarkers for Predicting Renal Dysfunction Progression in Autosomal Dominant Polycystic Kidney Disease. J Magn Reson Imaging 2021;53(2):564–576. [PubMed: 32969110]

231. Kazancioglu R, Ecder T, Altintepe L, et al. Demographic and clinical characteristics of patients with autosomal dominant polycystic kidney disease: a multicenter experience. Nephron Clin Pract 2011;117(3):c270–275. [PubMed: 20847569]

232. Torres VE, Wilson DM, Hattery RR, Segura JW. Renal stone disease in autosomal dominant polycystic kidney disease. Am J Kidney Dis 1993;22(4):513–519. [PubMed: 8213789]

233. Nishiura JL, Neves RF, Eloi SR, Cintra SM, Ajzen SA, Heilberg IP. Evaluation of nephrolithiasis in autosomal dominant polycystic kidney disease patients. Clin J Am Soc Nephrol 2009;4(4):838–844. [PubMed: 19339428]

234. Ozkok A, Akpinar TS, Tufan F, et al. Clinical characteristics and predictors of progression of chronic kidney disease in autosomal dominant polycystic kidney disease: a single center experience. Clin Exp Nephrol 2013;17(3):345–351. [PubMed: 23085781]

235. Alexander RT, Hemmelgarn BR, Wiebe N, et al. Kidney stones and kidney function loss: a cohort study. BMJ 2012;345:e5287. [PubMed: 22936784]

236. Brisbane W, Bailey MR, Sorensen MD. An overview of kidney stone imaging techniques. Nat Rev Urol 2016;13(11):654–662. [PubMed: 27578040]

237. Health Effects of Exposure to Low Levels of Ionizing Radiations: Time for Reassessment? Washington (DC); 1998.

238. Dellschaft NS, Hutchinson G, Shah S, et al. The haemodynamics of the human placenta in utero. PLoS Biol 2020;18(5):e3000676. [PubMed: 32463837]

239. Zhu A, Reeder SB, Johnson KM, et al. Quantitative ferumoxytol-enhanced MRI in pregnancy: A feasibility study in the nonhuman primate. Magn Reson Imaging 2020;65:100–108. [PubMed: 31655139]

240. Wu B, Li W, Guidon A, Liu C. Whole brain susceptibility mapping using compressed sensing. Magn Reson Med 2012;67(1):137–147. [PubMed: 21671269]

241. Liu T, Liu J, de Rochefort L, et al. Morphology enabled dipole inversion (MEDI) from a single-angle acquisition: comparison with COSMOS in human brain imaging. Magn Reson Med 2011;66(3):777–783. [PubMed: 21465541]

242. Li W, Wu B, Liu C. Quantitative susceptibility mapping of human brain reflects spatial variation in tissue composition. Neuroimage 2011;55(4):1645–1656. [PubMed: 21224002]

243. Neelavalli J, Jella PK, Krishnamurthy U, et al. Measuring venous blood oxygenation in fetal brain using susceptibility-weighted imaging. J Magn Reson Imaging 2014;39(4):998–1006. [PubMed: 24783243]

244. Yadav BK, Krishnamurthy U, Buch S, et al. Imaging putative foetal cerebral blood oxygenation using susceptibility weighted imaging (SWI). Eur Radiol 2018;28(5):1884–1890. [PubMed: 29247352]

245. Yadav BK, Buch S, Krishnamurthy U, et al. Quantitative susceptibility mapping in the human fetus to measure blood oxygenation in the superior sagittal sinus. Eur Radiol 2019;29(4):2017–2026. [PubMed: 30276673]

246. Sun T, Qu F, Yadav B, et al. Estimating cerebral venous oxygenation in human fetuses with ventriculomegaly using quantitative susceptibility mapping. Magn Reson Imaging 2021;80:21–25. [PubMed: 33845161]

247. Sun C, Ghassaban K, Song J, et al. Quantifying calcium changes in the fetal spine using quantitative susceptibility mapping as extracted from STAGE imaging. Eur Radiol 2022.

248. Vintzileos AM, Nioka S, Lake M, Li P, Luo Q, Chance B. Transabdominal fetal pulse oximetry with near-infrared spectroscopy. Am J Obstet Gynecol 2005;192(1):129–133. [PubMed: 15672014]

249. Benkert T, Feng L, Sodickson DK, Chandarana H, Block KT. Free-breathing volumetric fat/water separation by combining radial sampling, compressed sensing, and parallel imaging. Magn Reson Med 2017;78(2):565–576. [PubMed: 27612300]

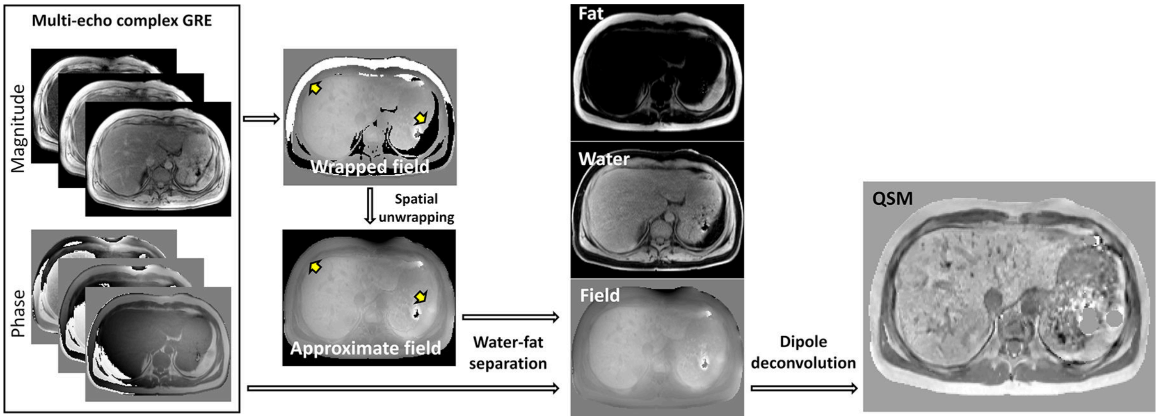

Figure 1.

Flowchart of QSM reconstruction in body applications. Susceptibility mapping requires acquisition and preservation of both magnitude and phase of standard complex gradient echo sequence. Water-fat separation is performed to generate a high-fidelity magnetic field map. Dipole deconvolution to solve the inverse field-to-source problem is performed as the final step

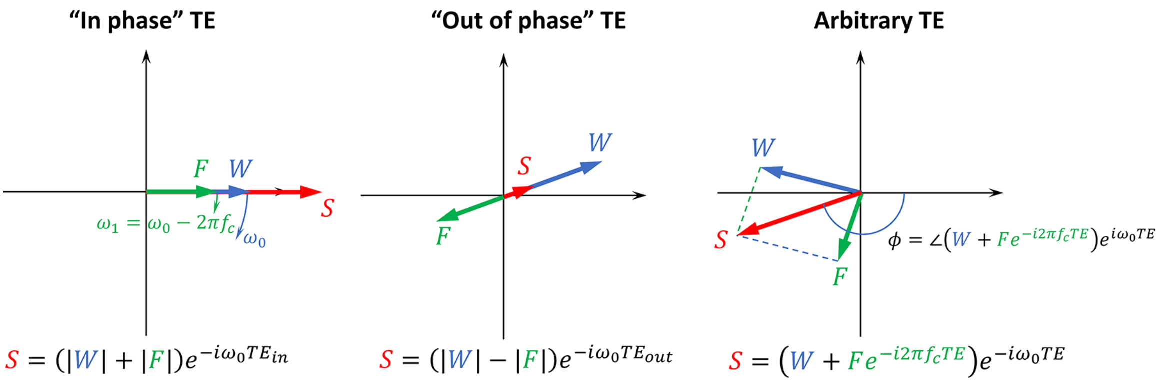

Figure 2.

Effects of chemical shift in field mapping. Signal vector diagram illustrating GRE phase behavior in presence of fat. Because of the chemical shift, signals of water (W, blue arrow) and fat (F, green arrow) experience different rates of phase accrual, ω_0 and ω_1; adding and subtracting images S acquired at strategically selected "In phase" and "out of phase" echo times, water and fat images can be generated. At an arbitrary echo time, relationship between the echo time and phase becomes nonlinear, and its dependence on chemical shift value can be exploited for estimation of water, fat images, and field mapping

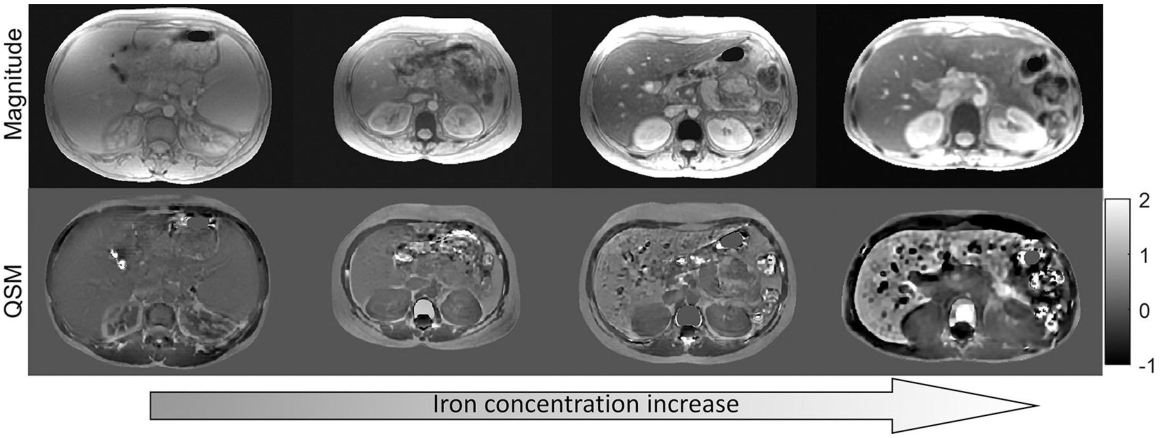

Figure 3.

Magnitude and QSM images in four thalassemia major patients. Higher degrees of iron overload manifest in gradual increase of liver parenchymal susceptibility, linearly proportional to iron concentration (adapted from (64))

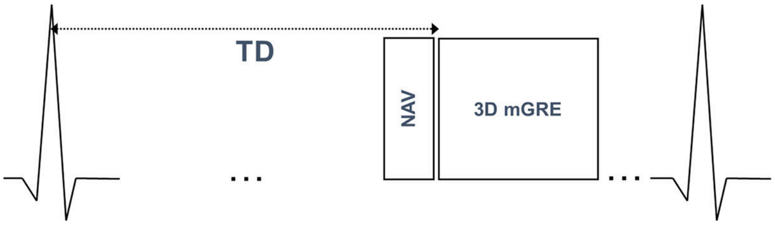

Figure 4.

Pulse sequence diagram for cardiac QSM. ECG triggered navigator 3D Cartesian multi-echo gradient echo free breathing acquisition

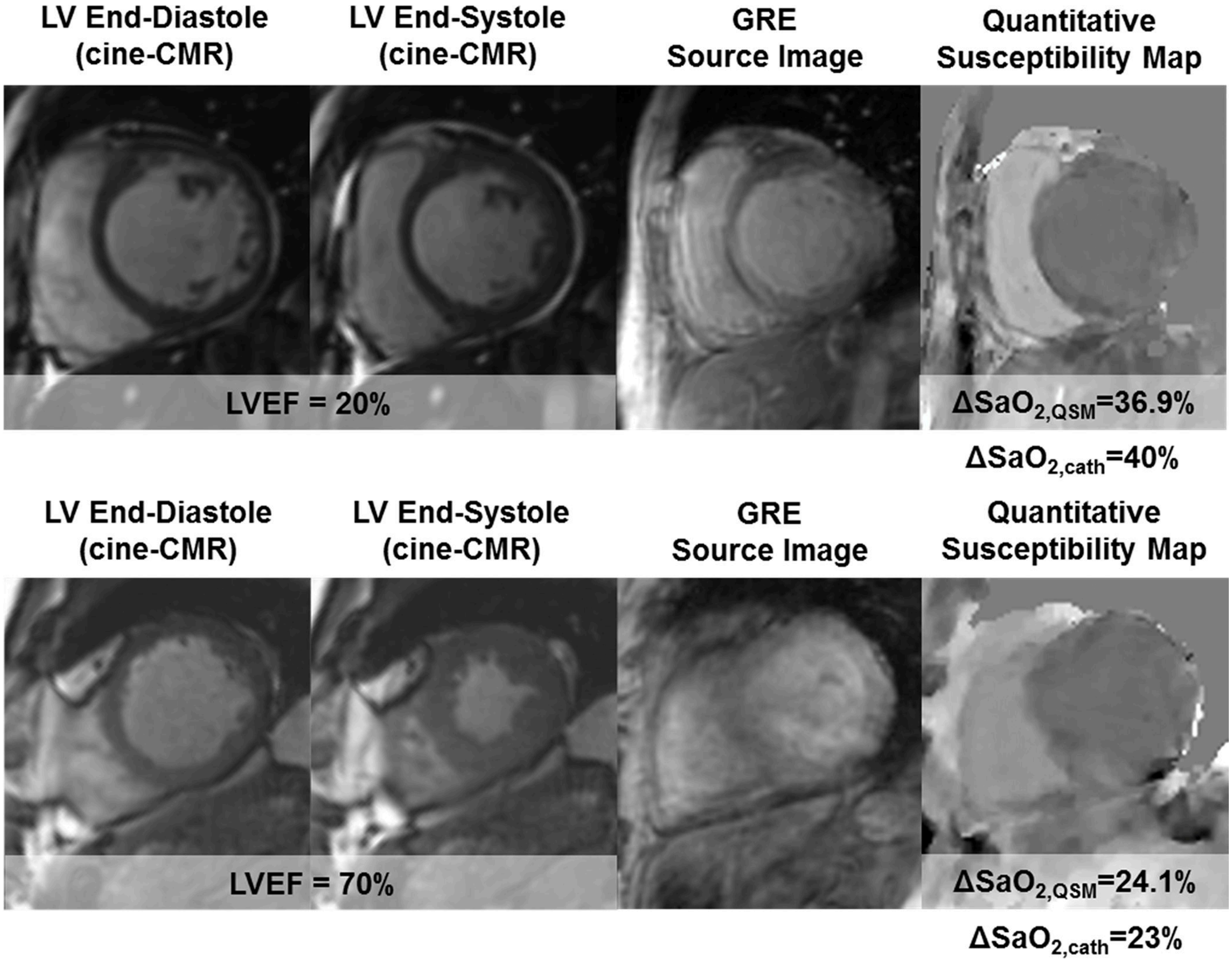

Figure 5.

Two representative examples of QSM maps in cardiac patients. In the top patient, who had severely reduced LV function (EF=20%), QSM measured a marked increase in ΔSO_2 (36.9%), which agreed well with invasive catheterization (40%). In the bottom patient, who had normal LV function (EF=70%), QSM measured ΔSO_2 (24.1%) was within normal limits and was similar to invasive data (23%). Reprinted with permission from (128)

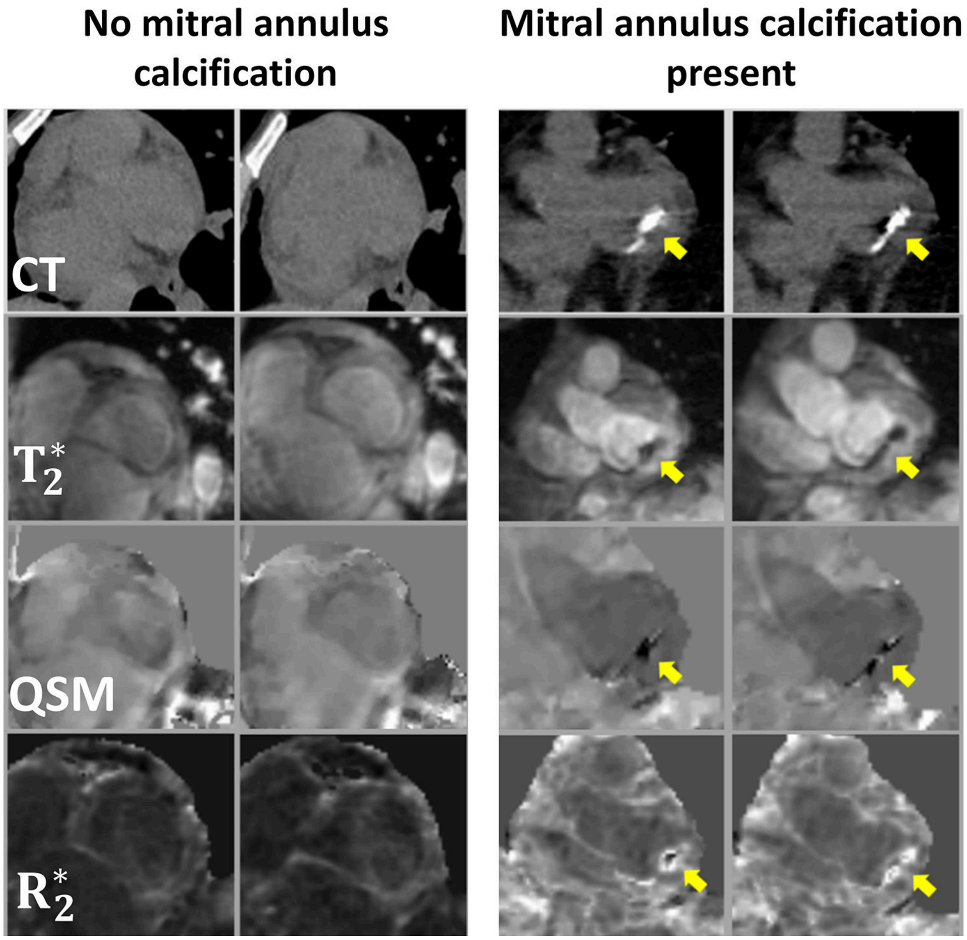

Figure 6.

QSM of mitral calcification. Representative examples of patients with and without MAC as visualized by CT and T_2^* weighted magnitude, QSM, and R_2^* pulse sequences on cardiac MRI. Note that CT evidenced calcium was found to correspond with presence and location of annular susceptibility on cardiac QSM. Reprinted with permission from (133).

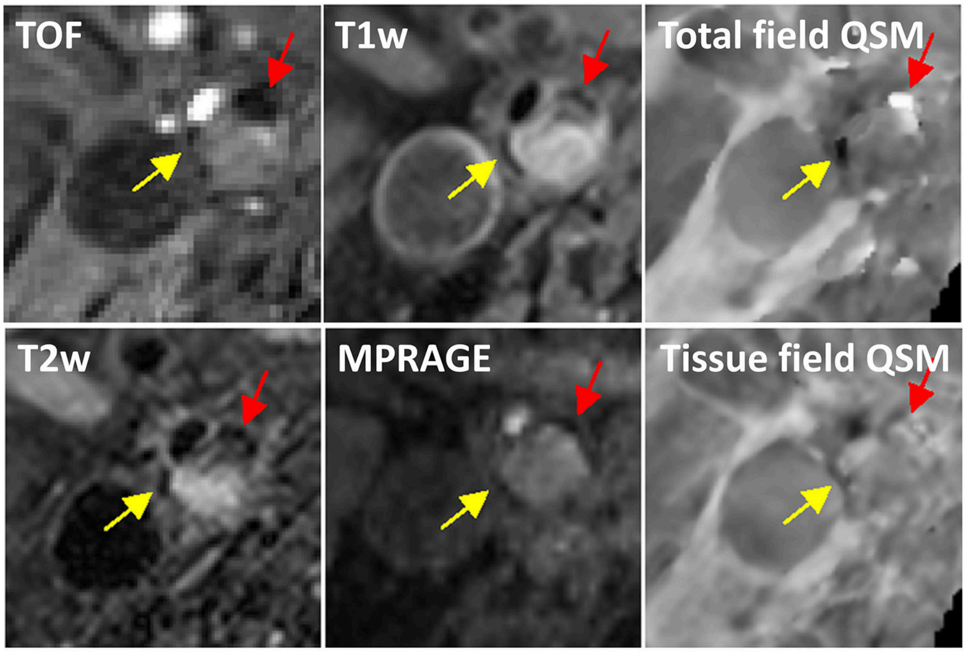

Figure 7.

Comparison between tissue and total field inversion QSM techniques. Two regions at the boundary of a large plaque from a 63-year-old carotid artery stenosis patient appear similarly hypointense on TOF, T_1w, T_2w, and MPRAGE images. On QSM reconstructed using total field inversion, one region has a strong diamagnetic appearance (yellow arrow), consistent with calcification, while the other region has strongly positive susceptibility indicative of an old hemorrhage with hemosiderin deposition (red arrow). This susceptibility contrast could not be seen well on QSM obtained with a tissue field inversion approach (adapted from (39))

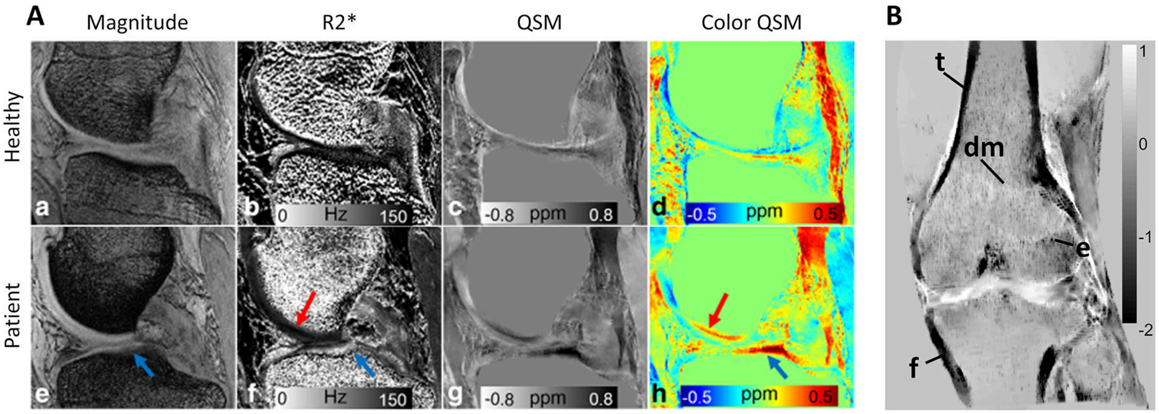

Figure 8.

QSM in MSK imaging. A) Medial cartilage in a healthy subject (a-d) and a patient with collagen damage (e-h). Patient magnitude and R_2^* images reveal signal alteration in the tibial plateau compared to the healthy control (arrows). Susceptibility map (h) reflects changes in cartilage composition in the affected regions (adapted from (167)). B) MIP of a whole knee joint QSM in a healthy subject demonstrating delineation of cortical areas of the femur (f) and tibia (t), the depiction of trabeculation, the epiphyseal line (e) and transition from diaphyseal to metaphyseal bone (dm) (adapted from (55))

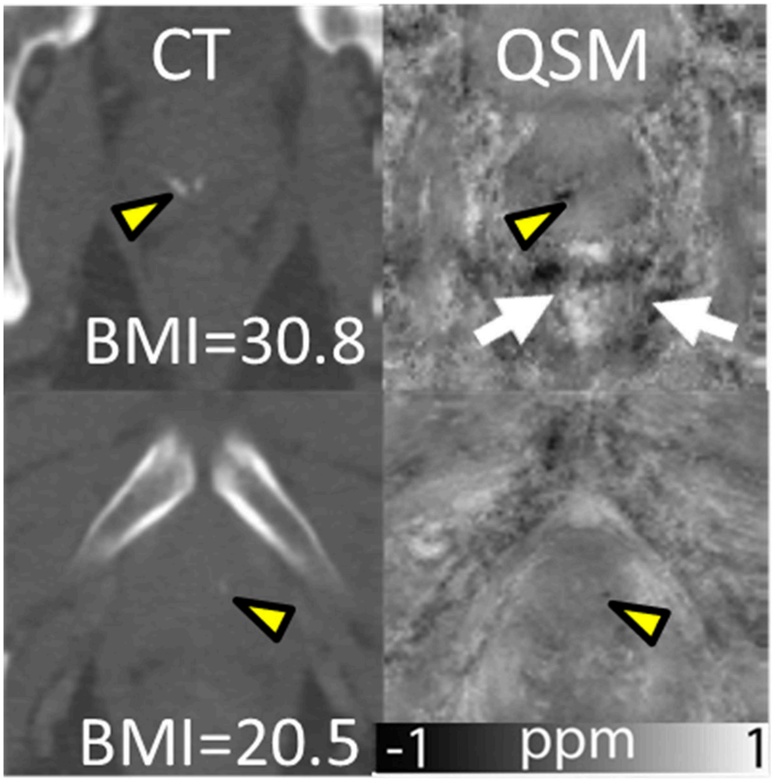

Figure 9.

QSM in prostate. Prostatic calcifications (yellow arrowheads) in CT images (first column), and susceptibility maps (second column). Motion/air artifacts and noise can be observed around the prostate (first row), indicated by arrows. Additionally, body mass index (BMI) of patients is provided (adapted from (46)).

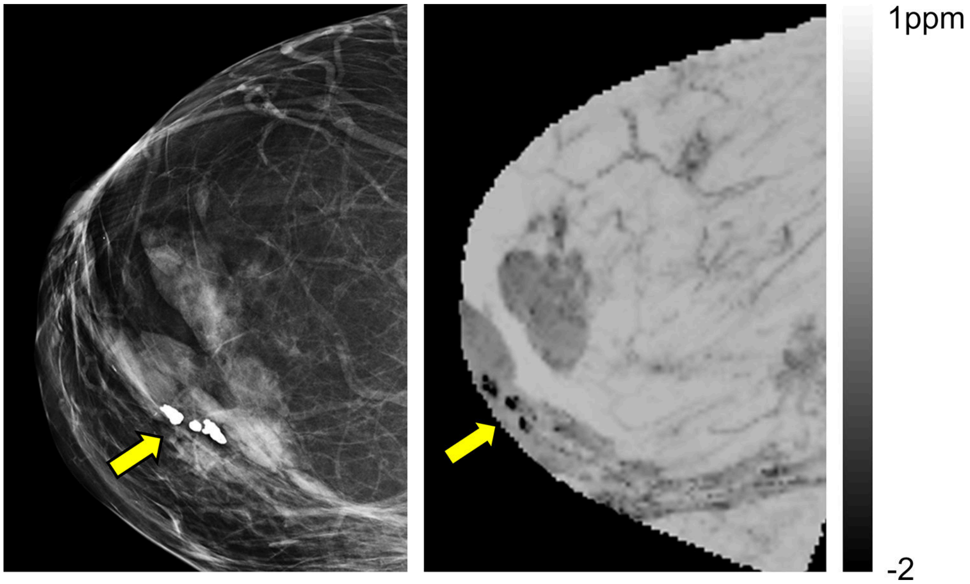

Figure 10.

QSM in breast. Mammogram (left) and QSM (right) of a breast in a female patient with calcified nodules. (adapted from (200)). QSM is able to unambiguously identify of calcifications, which appear hypo-intense due to their diamagnetic susceptibility

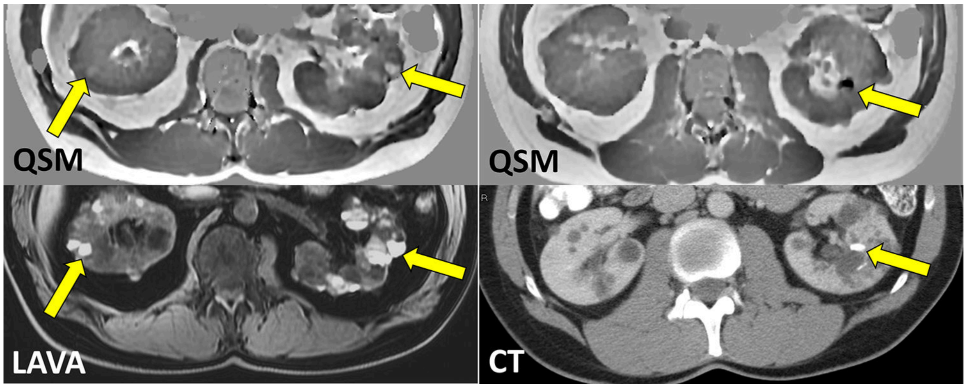

Figure 11.

Kidney QSM in ADPKD. A) Despite hyperintense appearance on 3D T_1w LAVA image, only few ADPKD cysts appear as paramagnetic on QSM (yellow arrows), indicating heterogeneity of cyst composition and non-specificity of T_1 hyperintensity to presence of hemorrhage and blood products. B) QSM allows detection of calcified kidney stones as confirmed by CT (unpublished data).

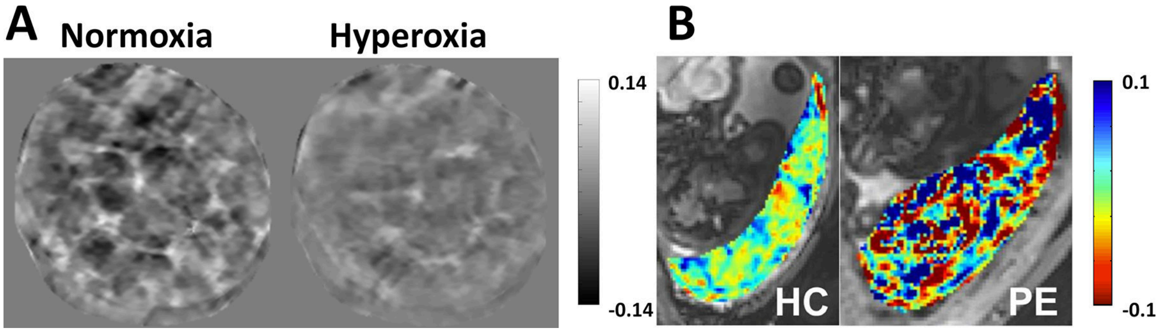

Figure 12.

QSM in placenta. A) Susceptibility maps (ppm) acquired in a healthy pregnancy (gestational age, 29 1/7 weeks) under normoxia and maternal hyperoxia induced by administration of 100% oxygen within the same scan session. Spatial variation of susceptibility was substantially reduced under hyperoxia. B. Susceptibility maps (ppm) acquired in a health pregnancy (left; gestational age, 28 6/7 weeks) and one complicated by preeclampsia (right; gestational age, 35 weeks). Susceptibility of the placenta associated with preeclampsia showed markedly increased spatial variation. Reprinted from (218, 219).